Energy Loss Optimization Method Considering the Time-varying Characteristics of Battery Energy Storage Systems

Gan Guo, Junhui Li, Gang Mu, *Fellow*, *IET*, and Gangui Yan, *Senior Member*, *CSEE*

***Abstract*—A time-varying optimization strategy for battery cluster power allocation is proposed to minimize energy loss in battery energy storage systems (BESS). First, the time-dependent loss characteristics of both storage and non-storage components in BESS are analyzed. Based on this analysis, steady-state and transient methods for evaluating battery loss are proposed. Second, considering the distinct time-varying characteristics of various BESS components, the load-rate vs. equivalent-efficiency curve and the current-loss power component gradient field are introduced as analytical tools. These tools facilitate the derivation of optimization path for both time-varying and time-invariant energy components of BESS. Building on this foundation, a time-varying optimization strategy for battery cluster power allocation is developed, aiming to minimize energy loss while fully accounting for the dynamic characteristics of BESS. Compared to real-time optimization, this strategy prioritizes global optimality in the time domain, mitigates the risk of dimensionality curse, and enhances BESS efficiency. Finally, a Simulink/Simscape model is established based on real-world data to simulate internal component losses within BESS. The effectiveness of the proposed strategy is validated under a peak shaving scenario. Results indicate that, after optimization, the annual operational loss of BESS is reduced by 2.40%, while the energy round-trip efficiency is improved by 0.59%.**

***Index Terms*—Battery energy storage system, battery cluster power allocation, efficiency, time-varying optimization.**

Received: November 15, 2024
Accepted: July 20, 2025
Published Online: November 1, 2025

Gan Guo, Junhui Li (corresponding author), Gang Mu, Gangui Yan are with the Key Laboratory of Modern Power System Simulation and Control & Renewable Energy Technology, Northeast Electric Power University, Jilin 132012, China (e-mail: guogan@outlook.com; lijunhui@neepu.edu.cn; mg@neepu.edu.cn; yangg@neepu.edu.cn).

DOI: 10.23919/PCMP.2024.000288

I. Introduction

Battery energy storage systems (BESS) play an increasingly critical role in modern power systems by improving grid reliability, enhancing operational flexibility, and facilitating the integration of renewable energy sources. As complex systems that convert electrical, thermal, and chemical energy, BESS efficiency is of paramount importance. Typically, large-scale lithium-ion BESS exhibit efficiencies ranging from 70% to 90% [1]–[3]. According to [4], the average monthly round-trip efficiency of US energy storage facilities is approximately 82%, while China's National Photovoltaic and Energy Storage Experimental Platform has documented a peak efficiency of 82.66% for $LiFePO_4$ BESS [5]. These findings indicate the potential for further efficiency improvements. Achieving higher efficiency necessitates an in-depth analysis of BESS component energy loss characteristics and the development of advanced control strategies. This study examines energy loss mechanisms in BESS, battery modeling methodologies, power conversion system (PCS) efficiency, battery cluster control, and time-varying optimization algorithms, providing a comprehensive review of existing advancements and research gaps.

Recent research has explored BESS efficiency across various storage types [6], [7], application scenarios [7]–[10], and control methods [11]–[13]. Studies have used engineering practices and physical experiments [10], [13], computer simulations [6], [8], [12], and hardware-in-the-loop simulations [9], [11]. Most works focus on external characteristics modeling, with less attention to internal component characteristics. References [11] and [12] model BESS loss via efficiency curves but overlook the dynamic characteristic of battery, treating BESS as time-invariant system. As a complex system with multiple energy conversions and component coupling, studies on BESS losses should focus more on the impact of the internal component characteristics on efficiency. In Li-ion BESS, main

energy losses stem from battery and PCS [14], [15], so the loss characteristics of these components determine the overall BESS efficiency.

Batteries are highly nonlinear, time-varying systems. Currently, modeling research spans thermal effects [16], [17], capacity degradation and aging [18]–[20], SoC estimation [21], and energy efficiency [22], [23]. Compared to electrochemical [16], [18] and neural network models [21], the equivalent circuit model offers a better balance of accuracy and complexity. Multi-order RC and PNGV models are more suitable for efficiency studies in power systems [24]. Research on charging strategies shows that constant current/voltage modes are simple but ignore battery dynamics, and thus reduce overall efficiency [25]. Variable current strategies, especially positive pulse current (PPC) charging [26]–[28], improve efficiency by avoiding lithium saturation and reducing polarization. However, these real-time control studies lack forecasting and planning, and ignore time-varying characteristics on efficiency. In peak shaving and renewable integration scenarios, predicting BESS input is crucial. As installed capacity and operation time increase, the cumulative effect of time-varying characteristics on efficiency cannot be ignored. Researches in [29] and [30] focus on time-varying optimization in microgrid, but BESS loss optimization remains unexplored. Thus, developing time-varying loss models and feasible optimization strategies are necessary to improve efficiency.

PCS is a major BESS component. Research has highlighted the prevalent challenge of low PCS efficiency under light-load conditions [31]–[34]. Reference [33] models PCS as a time-invariant system using experimental data to track maximum efficiency points. Reference [34] improves light-load efficiency by optimizing PCS structure, but is unsuitable for bidirectional power scenarios. Additionally, these modifications introduce control complexities, reduce component lifespan, and increase high-load losses [34]. Enhancing light-load efficiency of a single PCS inherently involves trade-offs.

Due to the parallel structure of multiple battery clusters in BESS, each cluster's PCS can execute different commands, allowing decoupled control. However, most studies assume balanced operation due to the complexity of imbalance control strategies. References [11] and [12] examine the impact of power flow distribution on the efficiency of parallel-connected cell strings within BESS. Additionally, control strategies for distributed energy storage [35], [36] and vehicle-to-grid (V2G) technology [37]–[39] provide references for parallel operation of battery clusters, validating the advantages of decentralized control. However, they also reveal common problems, such as in frequency regulation [11], black start [36], and automotive power batteries [37]–[39], where BESS typically employ real-time control rather than being pre-planned, thus often neglecting time-varying characteristics. Furthermore, their operational constraints differ significantly from internal battery clusters. Thus, it is necessary to conduct more research on coordination of battery clusters, while considering their operational characteristics.

To optimize BESS energy loss, appropriate algorithms must be applied based on the characteristics of the optimization model. Accounting for time-varying characteristics introduces high-dimensional solution spaces. Common heuristic algorithms, while widely adaptable and model-free [40], are prone to local optima and the curse of dimensionality in high-dimensional time varying problems [41]. To overcome these challenges, reference [42] introduces a kind of time-varying convex optimization problems and proposes algorithms based on online prediction in discrete and continuous time domains. References [29] and [30] apply time-varying algorithms to emission and economic dispatch in microgrids and smart grids, without being specifically to BESS. The optimization of time-varying problems in power systems is gaining increasing attention. This study incorporates BESS time-varying characteristics and proposes an original battery cluster power allocation strategy to optimize BESS energy loss. The study structure is shown in Fig. 1.

The main contributions of this study are as follows.

1) The study analyzes the loss characteristics of BESS components, innovatively modeled BESS energy loss as a time-varying process, and proposed methods for analyzing steady-state and transient battery losses.

2) Based on the differentiated time-varying characteristics of BESS components, the study evaluates the differences between time-varying and time-invariant systems in energy optimization. It proposes optimization paths for BESS based on the load ratio-equivalent efficiency curve and the current vs power loss component gradient field.

3) A time-varying optimization strategy for battery cluster power allocation is designed to minimize energy loss in BESS, prioritizing optimality in global time domain over real-time optimization.

4) A Simulink/Simcape simulation model is developed with real-world data to simulate energy losses of BESS components, assessing their magnitude, composition, and the impact of control strategies under peak shaving scenario.

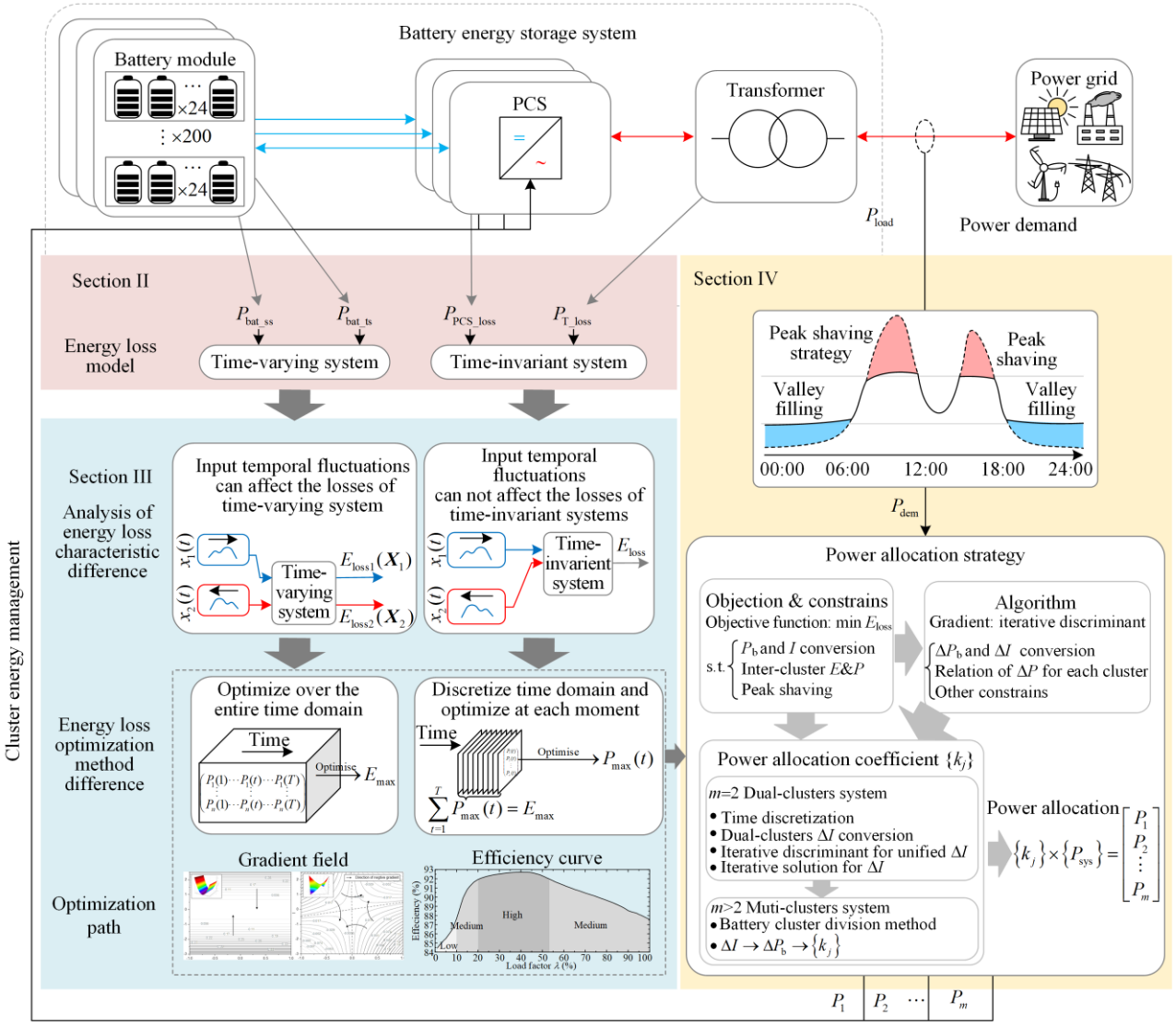

Fig. 1. Research structure overview diagram.

II. Time-Varying and Time-Invariant Characteristics of the BESS Loss Model

A. Basic Composition of ESS Energy Losses

This study aims to describe the fundamental time-varying characteristics of BESS using the most basic and general models. It focuses only on electrical losses, excluding the energy consumption of auxiliary equipment.

As shown in Fig. 1, the components of a BESS include transformers, AC/DC and DC/DC PCSs as non-storage components, and battery modules as energy storage components. A set of AC/DC and DC/DC PCS, and battery module form a battery cluster, while multiple clusters form a complete BESS. Various forms of energy conversion are involved among the components. A Sankey chart of energy flow between BESS and power grid is shown in Fig. 2.

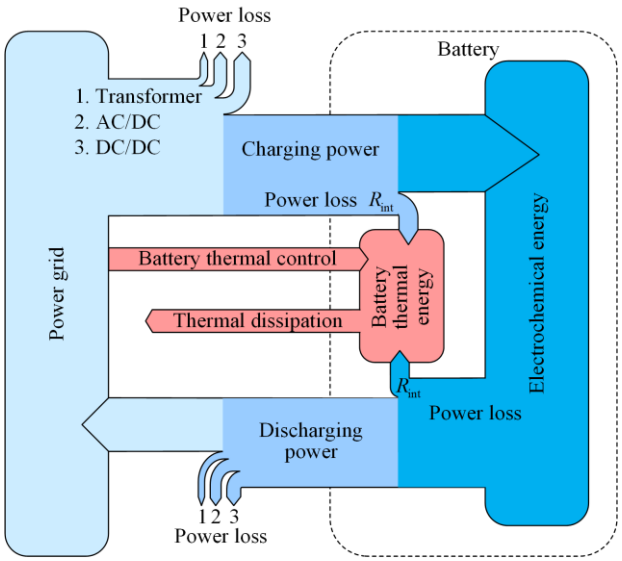

Fig. 2. Sankey chart of energy flow in BESS.

B. Time-invariant Nature of Non-energy Storage Components Loss Model

1) Transformer

According to transformer's T-type equivalent circuit model [43], the relationship between the power loss and the load rate β is established, as:

$$P_{\mathrm{TF\_loss}}(\beta) = P_{\mathrm{Fe}} + \beta^2 P_{\mathrm{kN}} \tag{1}$$

where P_{Fe} represents the excitation loss; and P_{kN} is the short-circuit loss, which can be considered constants for the same transformer. P_{Fe} which can be borne by the power grid, is not included in the BESS loss. The transformer parameters are set based on the reference values for a 5000 kVA transformer specified in GB/T 6451-2023, with $P_{\mathrm{Fe}} = 28.2$ kW, $P_{\mathrm{kN}} = 158$ kW. The power loss model of the transformer is a non-homogeneous, non-additive, and time-invariant system, where the loss is only related to instantaneous load power.

2) Power Converter System

The efficiency of PCS can be modeled as a function of the input [44]. Based on the measured data of the Hongsheng PWS1 50k PCS, the relationship between efficiency and load rate is fitted as:

$$\eta_{\mathrm{PCS}}(\beta) = a_0 + a_1\beta + a_2\beta^2 + a_3\beta^3 + a_4\beta^4 \tag{2}$$

where $a_0 = 0.7868$, $a_1 = 0.7955$, $a_2 = -2.073$, $a_3 = 2.137$, and $a_4 = -0.8137$. The rated power is P_{N} and load power is *P*. The load rate is defined as:

$$\beta \triangleq \frac{P}{P_{\mathrm{N}}}, \beta \in [0,1] \tag{3}$$

If the PCS is viewed with load power as input and loss power as output, it shows non-homogeneous, non-additive, and time-invariant characteristics. Its efficiency depends solely on the instantaneous input, demonstrating immediacy. Achieving optimal efficiency at each moment maximizes overall PCS efficiency over time. Therefore, analyzing PCS efficiency requires only examining the instantaneous input power.

C. Time-varying Nature of Energy Storage Components Loss Model

1) Time-varying Nature Between Battery Power and Battery Current

Large-scale BESS commonly use a nonlinear battery model with an RC circuit [45], reflecting basic dynamic and time-varying electrical characteristics. This study adopts the Thevenin equivalent model with a first-order RC circuit as shown in Fig. 3.

The state of charge (SoC) of the battery can be represented as *S*:

$$S(t) = \frac{1}{C_{\mathrm{N}}}\int_0^t I(\tau)\mathrm{d}\tau \tag{4}$$

where C_{N} is the ampere-hour capacity; and $S(t) \in [0,1]$.

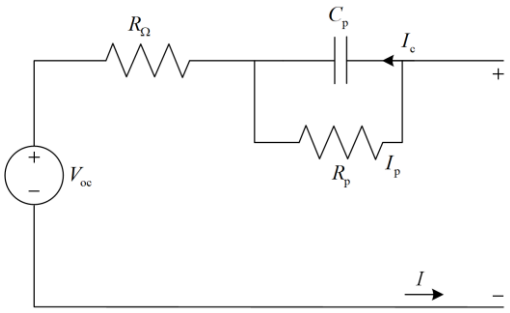

Fig. 3. Battery equivalent circuit model.

The battery's open-circuit voltage V_{oc} has a non-linear relationship with its $S(t)$. Based on multiple pulse discharge experiments conducted on several Shenhang LR12500SA lithium batteries and averaging the results, a *S*-V_{oc} relation curve has been obtained, as shown in Appendix A. It can be fitted into the following polynomial:

$$V_{\mathrm{oc}}(S) = b_0 + b_1 S + b_2 S^2 + b_3 S^3 \tag{5}$$

where the coefficients are determined as: $b_0 = 2.484$ V, $b_1 = 2.608$ V, $b_2 = -5.252$ V, $b_3 = 3.603$ V.

The relationship between the battery terminal power $P_{\mathrm{b}}(t)$ and current $I(t)$ is given by:

$$P_{\mathrm{b}}(t) = I(t)\left[V_{\mathrm{oc}}(S) + I(t)R + \frac{1}{C_{\mathrm{p}}}\int_0^t I(\tau)\mathrm{e}^{\frac{\tau - t}{R_{\mathrm{p}}C_{\mathrm{p}}}}\mathrm{d}\tau\right] \tag{6}$$

From (6), if the battery's charge/discharge power is the input and the current is the output, the presence of time-integral components makes the power-to-current process time-varying.

2) Time-varying Nature Between Battery Power and Steady-state Component

Battery power loss $P_{\mathrm{bat\_loss}}$ is defined as follows:

$$P_{\mathrm{bat\_loss}} = P_{\mathrm{bat\_ro}} + P_{\mathrm{bat\_rp}} = R_\Omega I^2 + R_{\mathrm{P}} I_{\mathrm{P}}^2 \tag{7}$$

where $P_{\mathrm{bat\_ro}}$ is the power loss of ohmic internal resistance R_Ω; and $P_{\mathrm{bat\_rp}}$ is the power loss of polarization resistance R_{p}.

The expression for the relationship between the polarization current I_{p} and the terminal current *I* is:

$$I_{\mathrm{p}} = I - \int_0^t I'(\tau)\mathrm{e}^{\frac{\tau - t}{R_{\mathrm{P}}C_{\mathrm{P}}}}\mathrm{d}\tau \tag{8}$$

Substituting (8) into (7) yields:

$$P_{\mathrm{bat\_loss}} = R_\Omega I^2 + R_{\mathrm{p}} I^2 + R_{\mathrm{p}}\left(\int_0^t I'(\tau)\mathrm{e}^{\frac{\tau - t}{R_{\mathrm{P}}C_{\mathrm{P}}}}\mathrm{d}\tau\right)^2 - 2R_{\mathrm{p}} I\int_0^t I'(\tau)\mathrm{e}^{\frac{\tau - t}{R_{\mathrm{P}}C_{\mathrm{P}}}}\mathrm{d}\tau \tag{9}$$

Since the battery model includes an RC transient circuit, the battery power loss can be divided into

steady-state and transient parts. The steady-state loss component $P_{\text{bat\_ss}}$ is extracted as follows:

$$P_{\text{bat\_ss}}(I)=P_{\text{bat\_ro}}(I)+I^2R_{\text{P}}=I^2(R_{\Omega}+R_{\text{P}}) \tag{10}$$

From (10), $P_{\text{bat\_ss}}$ is always positive, representing the power loss from the load current through the battery's internal resistance, determined solely by the terminal current I. With I as the input and $P_{\text{bat\_ss}}$ as the output, the model is non-homogeneous, non-additive, and time-invariant. Considering that efficiency optimization is achieved by power allocation among battery clusters, with BESS total charge/discharge power P_{sys} as the input and $P_{\text{bat\_ss}}$ as the output, the model is non-homogeneous, non-additive, and time-varying.

3) Time-varying Nature Between Battery Power and Transient Component

Subtracting (10) from (9), the transient power loss component $P_{\text{bat\_ts}}$ of the battery is extracted as follows:

$$P_{\text{bat\_ts}}(t,I,I')=P_{\text{bat\_rp}}(t,I,I')-I^2R_{\text{P}}=R_{\text{P}}\left(\int_0^t I'(\tau)\mathrm{e}^{\frac{\tau-t}{R_{\text{P}}C_{\text{P}}}}\mathrm{d}\tau\right)^2-2R_{\text{P}}I\int_0^t I'(\tau)\mathrm{e}^{\frac{\tau-t}{R_{\text{P}}C_{\text{P}}}}\mathrm{d}\tau \tag{11}$$

In (11), the integral part gradually decays to zero as I reaches steady state, with the rate of decay determined by the time constant $R_{\text{P}}C_{\text{P}}$. The integral part represents the polarization capacitor current I_{c}:

$$I_{\text{c}}=\int_0^t I'(\tau)\mathrm{e}^{\frac{\tau-t}{R_{\text{P}}C_{\text{P}}}}\mathrm{d}\tau \tag{12}$$

The magnitude of I_{c} is always smaller than I. When I fluctuates, I_{c} will either divert or compensate I_{P}, smoothing its fluctuations. The sign of $P_{\text{bat\_ts}}$ means:

1) $P_{\text{bat\_ts}}>0$, current compensation by C_{P} increases the polarization resistance power loss.

2) $P_{\text{bat\_ts}}<0$, current diversion by C_{P} reduces the polarization resistance power loss.

As defined in (11), the time integral of $P_{\text{bat\_ts}}$ is not equal to the energy of C_{P}, so it can be a non-zero value. $P_{\text{bat\_ts}}$ involves multiple variables accumulating over time, showing temporal accumulation characteristic. Thus, with I as the input and $P_{\text{bat\_ts}}$ as the output, its power loss model is non-homogeneous, non-additive, and time-varying. Similarly, P_{b} is taken as the input.

III. Impact of BESS Time-varying and Time-invariant Characteristics on Energy Loss Optimization Paths

A. Energy Loss Differences: Time-invariant vs. Time-varying Systems

1) Time-varying Relationships among Variables

The time-varying relationships among the main variables are summarized in Fig. 4.

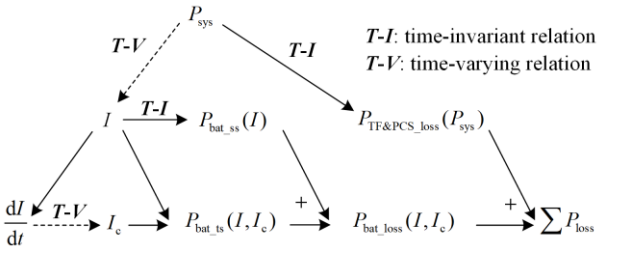

Fig. 4. Time-varying relationships among major variables.

As shown in Fig. 4, non-storage components, such as transformers and PCS, have a time-invariant path from system charge/discharge power (P_{sys}) to power losses of the transformer and PCS ($P_{\text{TF\&PCS\_loss}}$). However, for storage components, such as battery modules, the path from P_{sys} to battery loss ($P_{\text{bat\_loss}}$) involves both time-invariant and time-varying processes. From the battery's direct input variable I, the path leading to $P_{\text{bat\_ss}}$ remains time-invariant, whereas the path to $P_{\text{bat\_ts}}$ is time-varying.

2) Energy Loss Characteristics of Time-invariant Systems

Suppose there are two discrete input signal sets, x_1 and x_2, with identical elements but different time sequences, i.e.:

$$\begin{cases}x_1=x_2\\ x_1(t)\neq x_2(t),\ t\in[0,T]\end{cases} \tag{13}$$

It can be inferred that the integrals of both signals over the same period are equal, i.e.:

$$\int_0^T x_1(t)\mathrm{d}t=\int_0^T x_2(t)\mathrm{d}t \tag{14}$$

When signals x_1 and x_2 are input into time-varying and time-invariant systems, the outputs of these systems are different, as shown in Fig. 5.

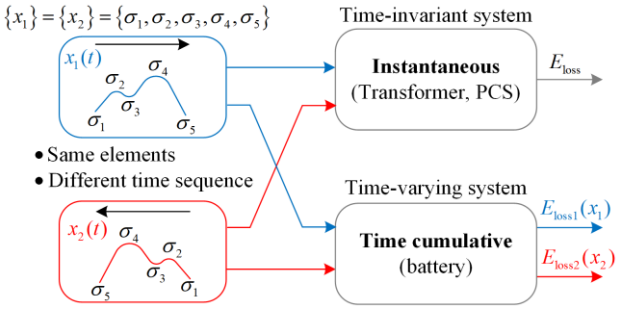

Fig. 5. Differences in loss characteristics between time-varying and time-invariant systems.

If signals x_1 and x_2 are input into a time-invariant system, temporal fluctuations of signals do not affect the output due to the instantaneous input-output relationship, so they produce the same result. For example, assuming signals x_1 and x_2 in Fig. 5 satisfy (13), the temporally ordered signal elements are:

$$\begin{matrix} & t=t_1 & t_2 & t_3 & t_4 & t_5 \\ \begin{cases} x_1(t)=\{\sigma_1,\sigma_2,\sigma_3,\sigma_4,\sigma_5\} \\ x_2(t)=\{\sigma_5,\sigma_4,\sigma_3,\sigma_2,\sigma_1\} \end{cases} & & & & & \end{matrix} \tag{15}$$

If $E_{\text{loss}}=E(\sigma)$ represents the system function, then for a time-invariant system, the final output loss energies E_{loss1} and E_{loss2} satisfy the following relationship:

$$\begin{cases} E_{\text{loss1}}=E(\sigma_1)+E(\sigma_2)+E(\sigma_3)+E(\sigma_4)+E(\sigma_5) \\ E_{\text{loss2}}=E(\sigma_5)+E(\sigma_4)+E(\sigma_3)+E(\sigma_2)+E(\sigma_1) \end{cases} \tag{16}$$

Therefore, the final output is independent of the timing sequence of the input signals. The loss energies obtained by x_1 and x_2 within the same time domain are identical, i.e., $E_{\text{loss1}}=E_{\text{loss2}}$.

Loss models of transformers, AC/DC and DC/DC PCSs are immediate and memoryless when $P_{\text{sys}}(t)$ is the input. This means the power loss at time t depends only on the current input $P_{\text{sys}}(t)$, regardless of previous input changes. For time-invariant components, the loss is solely determined by the input signal's magnitude and is unaffected by its temporal fluctuations. Any input signal satisfying condition (13) results in the same energy loss.

3) Energy Loss Characteristics of Time-varying Systems

Unlike time-invariant systems, the output of time-varying systems depends on the accumulated input value over time. Thus, temporal fluctuations in the input signals affect the system's output. Consequently, energy losses E_{loss1} and E_{loss2} resulting from different input signals $S_1(t)$ and $S_2(t)$ over the same period will not be consistent.

$$\begin{cases} E_{\text{loss1}}=E(\sigma_1)+E(\sigma_1,\sigma_2)+E(\sigma_1,\sigma_2,\sigma_3)+ \\ \qquad E(\sigma_1,\sigma_2,\sigma_3,\sigma_4)+E(\sigma_1,\sigma_2,\sigma_3,\sigma_4,\sigma_5) \\ E_{\text{loss2}}=E(\sigma_5)+E(\sigma_5,\sigma_4)+E(\sigma_5,\sigma_4,\sigma_3)+ \\ \qquad E(\sigma_5,\sigma_4,\sigma_3,\sigma_2)+E(\sigma_5,\sigma_4,\sigma_3,\sigma_2\sigma_1) \end{cases} \tag{17}$$

Therefore, different timing sequences of the input signals lead to different loss energies within the same time domain, i.e., $E_{\text{loss1}}\neq E_{\text{loss2}}$.

Similar to the above analysis, when P_{sys} is the input, the battery loss model accumulates over time and exhibits memory characteristics. The power loss at time t depends on both the current input and the cumulative input before time t, reflecting the influence of both the input magnitude and its temporal fluctuations on the battery loss.

B. Energy Loss Optimization for Time-Invariant Energy Systems

1) Energy Loss Optimization Concept Without Considering Time-varying Factors

Power allocation is achieved by adjusting the allocation coefficients k for each battery cluster, subject to the following constraint at any time t:

$$\begin{cases} \sum_{i=1}^{m} k_i(t)=1 \\ 0\leqslant k_i(t)\leqslant 1 \end{cases} \tag{18}$$

where m is the total number of battery clusters; and k_i is the power allocation coefficient for the ith battery cluster.

In discrete time domain, power allocation coefficients are represented by matrix $\boldsymbol{K}$. Rows m denote battery clusters, and columns T denote time length. Pre-planned matrix $\boldsymbol{K}$ allocates power demand $P_{\text{sys}}(t)$ of BESS, resulting in terminal power $\boldsymbol{K}\times P_{\text{sys}}(t)$ for each cluster at time t. Optimization of BESS losses is achieved by adjusting matrix $\boldsymbol{K}$, described as:

$$\begin{matrix} & 1 & \cdots & t & \cdots & T \\ 1 \\ \vdots \\ m \end{matrix}\begin{bmatrix} k_{11} & \cdots & k_{1t} & \cdots & k_{1T} \\ \vdots & & \vdots & & \vdots \\ k_{m1} & \cdots & k_{mt} & \cdots & k_{mT} \end{bmatrix}\times\begin{bmatrix} P_{\text{sys}}(1) & & \\ & \ddots & \\ & & P_{\text{sys}}(T) \end{bmatrix}=$$
$$\sum_{t=1}^{T}\begin{bmatrix} 0 & \cdots & k_{1t}P_{\text{sys}}(t) & \cdots & 0 \\ \vdots & & \vdots & & \vdots \\ 0 & \cdots & k_{mt}P_{\text{sys}}(t) & \cdots & 0 \end{bmatrix}\xrightarrow[\text{input BESS}]{\text{Optimise}[k]}E_{\max} \tag{19}$$

As previously mentioned, the temporal fluctuation of the input signal in a time-invariant system does not affect the output. Therefore, optimizing a time-invariant system can be decomposed into optimizing each time segment independently. By summing the optimal results across all time segments, the global optimal solution can be achieved. Therefore, the energy optimization problem for a time-invariant system can be simplified to an instantaneous power optimization problem, which is formulated as:

$$\left.\begin{array}{l} \text{Parallel optimisation} \\ \text{Time is 1}\ \begin{bmatrix} k_{11}P_{\text{sys}}(1) \\ k_{21}P_{\text{sys}}(1) \\ \vdots \\ k_{m1}P_{\text{sys}}(1) \end{bmatrix}\xrightarrow[\text{input BESS}]{\text{Optimise } k_{11}-k_{m1}}P_{\max}(1) \\ \vdots \qquad\qquad \vdots \\ \text{Time is } t\ \begin{bmatrix} k_{1t}P_{\text{sys}}(t) \\ k_{2t}P_{\text{sys}}(t) \\ \vdots \\ k_{mt}P_{\text{sys}}(t) \end{bmatrix}\xrightarrow[\text{input BESS}]{\text{Optimise } k_{1t}-k_{mt}}P_{\max}(t) \\ \vdots \qquad\qquad \vdots \\ \text{Time is } T\ \begin{bmatrix} k_{1T}P_{\text{sys}}(T) \\ k_{2T}P_{\text{sys}}(T) \\ \vdots \\ k_{mT}P_{\text{sys}}(T) \end{bmatrix}\xrightarrow[\text{input BESS}]{\text{Optimise } k_{1T}-k_{mT}}P_{\max}(T) \end{array}\right\}\Rightarrow$$
$$\sum_{t=1}^{T}P_{\max}(t)=E_{\max} \tag{20}$$

Mathematically, allocation coefficient matrix $\boldsymbol{K}$ vertically splits into allocation coefficient vectors for each

time point, without the temporal correlation. This allows for parallel optimization (e.g., parfor in MATLAB) of power at each time point, enhancing solution speed. At any time t, achieving full power allocation among m battery clusters requires at least $(m-1)$ independent allocation coefficients. They can be successively configured in groups using a splitting grouping method, simplifying the optimization into multiple one-dimensional variable problems.

2) Optimization Path

The time-invariant components in the BESS include transformers, AC/DC and DC/DC PCSs. The optimization path of the time-invariant system can be observed through the load rate-equivalent efficiency curve shown in Fig. 6.

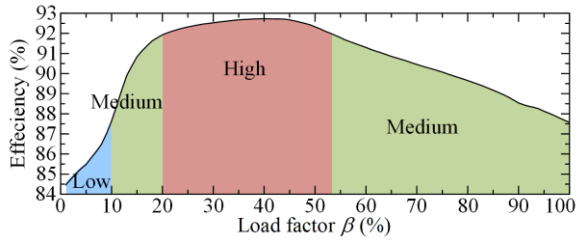

Fig. 6. Load-rate vs. equivalent-efficiency curve.

The curves are obtained based on the time-invariant components loss simulation constructed from transformer and PCS models. The input power of the simulation model increases uniformly from 0 to 50 kW, while the output power is recorded simultaneously. Efficiency is calculated as the output-to-input power ratio. The load factor represents the ratio of the input power to the rated power. This curve reflects the load-dependent efficiency pattern of the time-invariant subsystem in the BESS, composed of the transformer and PCS.

The PCS contributes most of BESS energy losses, because of its low efficiency under light load condition. Optimization is to adjust input power to operate within the high-efficiency range of the curve. Managing input power for each battery cluster must meet BESS power and SoC constraints, as detailed in Section IV.

C. Energy Loss Optimization for Time-varying Energy Systems

1) Energy Loss Optimization Concept with Time-varying Factors

As described in Section III, both the magnitude and fluctuation of the input signal affect the output of the time-varying system. If optimization still follows (20), the sum of the optimal instantaneous powers will only be less than or equal to the global optimal solution, i.e.:

$$\sum_{t=1}^{T} P_{\max}(t) \leqslant E_{\max} \tag{21}$$

Therefore, optimizing energy for a time-varying system presents a continuous-time energy planning problem. Unlike in time-invariant systems, optimization cannot be divided into discrete time intervals, and the temporal information of allocation coefficient matrix $\boldsymbol{K}$ must be considered to account for time correlation. Figure 7 illustrates the differences in energy optimization between time-varying and time-invariant systems.

Although the allocation coefficient matrix $\boldsymbol{K}$ in a time-varying system cannot be decomposed into vectors for each time point as in a time-invariant system, the $(m-1)$ independent allocation coefficients at any time t can still be configured sequentially using splitting grouping method. Thus, the minimum solution space dimension equals the number of time points (T), as shown in Fig. 7.

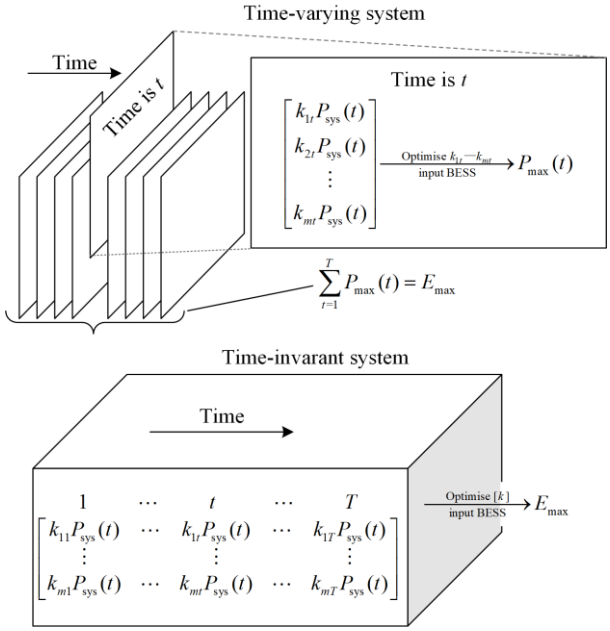

Fig. 7. Differences in energy optimization strategies between time-varying and time-invariant systems.

2) Optimization Path

Current distribution directly affects battery energy losses. The optimization path for time-varying component can be observed through the current-power gradient field, as shown in Fig. 8. As seen, the contour values represent the magnitude of $P_{\text{bat\_ss}}$ and $P_{\text{bat\_ts}}$, with I and I_{c} as the vertical and horizontal axes. Also, a 3D surface of gradient field is in the top left. Arrows point in the direction of the negative gradient, where $P_{\text{bat\_ss}}$ and $P_{\text{bat\_ts}}$ decrease.

For quantitative analysis of the current distribution differences in Section V, the $P_{\text{bat\_ts}}$ gradient field is divided into four quadrants based on the signs of $P_{\text{bat\_ts}}$ and I_{c}. The quadrant division rules are listed in Table I.

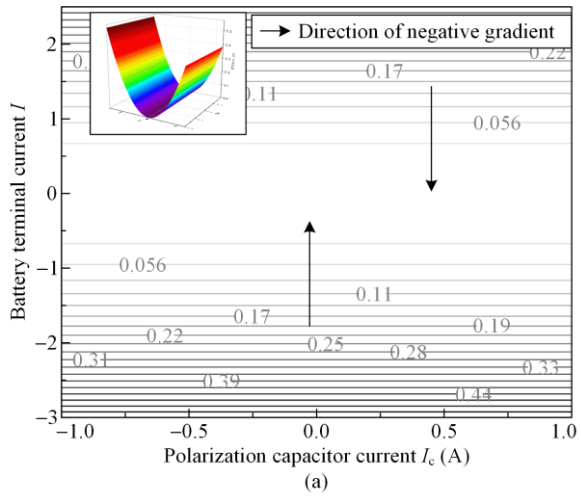

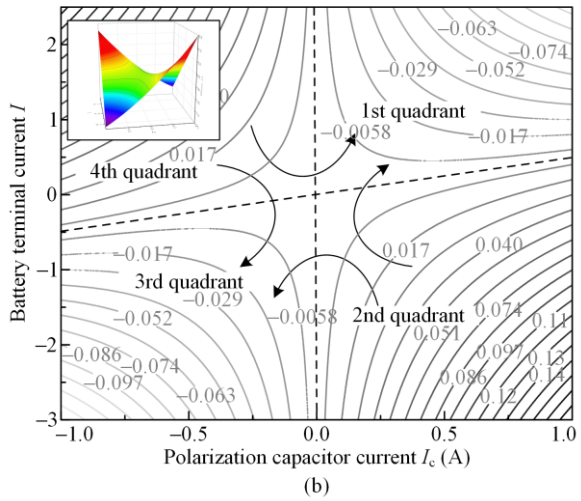

Fig. 8. Battery power loss gradient field. (a) Current vs. $P_{\text{bat\_ss}}$ gradient field. (b) Current vs. $P_{\text{bat\_ts}}$ gradient field.

TABLE I
QUADRANT DIVISION RULES

Variant	Q1	Q2	Q3	Q4	Quadrant boundary
$P_{\text{bat\_ts}}$	< 0	> 0	< 0	> 0	= 0
I_c	< 0	< 0	> 0	> 0	= 0

From Fig. 8, adjusting the current operating points along the negative gradient direction can effectively reduce power components. $P_{\text{bat\_ss}}$ is influenced by the magnitude of P_{sys} but remains unaffected by its rate of change. Given that P_{sys} must satisfy power constraints, the optimization potential for $P_{\text{bat\_ss}}$ is inherently limited. In contrast, $P_{\text{bat\_ts}}$ is dependent on both the magnitude and change rate of P_{sys}. Optimizing the distribution of input power fluctuations across battery clusters can significantly enhance the regulation of $P_{\text{bat\_ts}}$. Furthermore, the *P-I* relationship influences the complexity of the optimization path, as will be elaborated in Section IV.

IV. BATTERY CLUSTER POWER ALLOCATION FOR ENERGY LOSS OPTIMIZATION CONSIDERING TIME-VARYING CHARACTERISTICS OF LOSS MODEL

A. BESS Operating Scenario

This study is based on the peak shaving scenario. Energy storage participates in peak shaving control strategy overview is shown in Fig. 9.

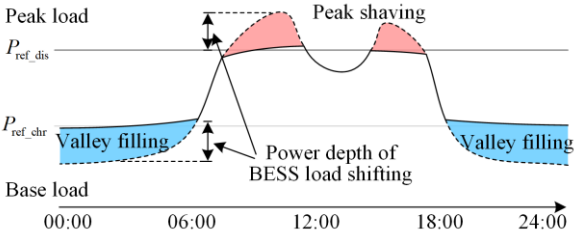

Fig. 9. Strategy overview of peak load regulation with BESS.

The system plans the system power $P_{\text{sys}}(t)$ (positive for charging, negative for discharging) as follows:

$$P_{\text{sys}}(t)=\begin{cases} P_{\text{N}},\ P_{\text{load}}(t)\in\left(0,P_{\text{ref\_chr}}-P_{\text{N}}\right] \ \&\ S\in[0,1) \\ P_{\text{ref\_chr}}-P_{\text{load}}(t),\ P_{\text{load}}(t)\in\left(P_{\text{ref\_chr}}-P_{\text{N}},P_{\text{ref\_chr}}\right) \\ \qquad\qquad \&\ S\in[0,1) \\ P_{\text{ref\_dis}}-P_{\text{load}}(t),\ P_{\text{load}}(t)\in\left(P_{\text{ref\_dis}},P_{\text{ref\_dis}}+P_{\text{N}}\right) \\ \qquad\qquad \&\ S\in(0,1] \\ -P_{\text{N}},\ P_{\text{load}}(t)\in\left[P_{\text{ref\_dis}}+P_{\text{N}},+\infty\right) \&\ S\in(0,1] \\ 0,\ \text{other conditions} \end{cases} \tag{22}$$

where P_{load} is the power load of system; P_{N} is BESS rated power; $P_{\text{ref\_chr}}$ is the valley load charging reference limit; and $P_{\text{ref\_dis}}$ is the peak load discharging reference limit.

According to the day-ahead peak shaving plan, BESS charge/discharge power must adhere to capacity constraints, ensuring daily energy balance [46], i.e.:

$$\begin{cases} \int_{T_{\text{c\_chr}}} \max\left(P_{\text{sys}}(t),0\right)\text{d}t \leqslant E_{\text{N}} \\ \int_{24\text{ h}} P_{\text{sys}}(t)\text{d}t = 0 \end{cases} \tag{23}$$

where $T_{\text{c\_chr}}$ represents any continuous charging period within 24 hours and E_{N} is BESS rated energy capacity.

If the capacity constraints are exceeded, the peak and valley load adjustment targets $P_{\text{ref\_chr}}$ and $P_{\text{ref\_dis}}$ need to be readjusted.

B. Objective Function and Constraints

1) Objective Function

Maximizing electrochemical energy E in batteries means minimizing energy loss of the entire system. Over the period T, the objective function depends solely on the decision variable $I_j(t)$, constants α, and C_{N}, i.e.:

$$\max_{I_j} E(t, I_j) = \sum_{j=1}^{m} \int_0^t I_j(s) \left[\begin{array}{l} \alpha_0 + \dfrac{\alpha_1}{C_{\mathrm{N}}} \left(\int_0^s I_j(\tau) \mathrm{d}\tau \right) \cdots + \\ \dfrac{\alpha_3}{C_{\mathrm{N}}^3} \left(\int_0^s I_j(\tau) \mathrm{d}\tau \right)^3 \end{array} \right] \mathrm{d}s \tag{24}$$

2) Battery Cluster Power and Current Constraint

The power $P_j(t)$ and the current $I_j(t)$ of each battery cluster need to satisfy the following constraint:

$$P_j(t) \times \eta_{j,\mathrm{PCS}}(t) = I_j(t) \times \left[V_j(S) + I_j(t) R_\Omega + \frac{1}{C_{\mathrm{P}}} \int_0^t I_j(\tau) \mathrm{e}^{\frac{s-t}{R_{\mathrm{P}} C_{\mathrm{P}}}} \mathrm{d}\tau \right] \tag{25}$$

where $\eta_{j,\mathrm{PCS}}$ is the PCS efficiency of the jth battery cluster.

The battery cluster power can be restored from $I_j(t)$ as seen in (25), and then the allocator coefficient matrix $\boldsymbol{K}$ can be obtained using (19).

3) Inter-cluster Energy Constraints

$\boldsymbol{K}$ satisfies (18), and the SoC constrains the power of each battery clusters:

$$P_j(t) = k_j \times P_{\mathrm{sys}}(t) \times \Theta(t), \quad k_j \in [0,1] \tag{26}$$

$$\Theta(t) \triangleq \begin{cases} 0, & P_j(t) > 0 \ \& \ S(t) = S_{\max} \\ 0, & P_j(t) < 0 \ \& \ S(t) = S_{\min} \\ 1, & \text{others} \end{cases} \tag{27}$$

where $\Theta(t)$ is the power correction factor by the SoC constraint. In this case, the depth of charge, $S_{\max} = 1$ and $S_{\min} = 0$.

Charging power of each battery cluster must not exceed its rated power P_{N}:

$$-P_{\mathrm{N}} \leqslant P_j(t) \leqslant P_{\mathrm{N}} \tag{28}$$

At time t, the sum of the power of each battery cluster $P_j(t)$ equals the total power demand of the BESS $P_{\mathrm{sys}}(t)$:

$$\sum_{j=1}^{m} P_j(t) = P_{\mathrm{sys}}(t) \tag{29}$$

4) Peak Shaving Constraints for BESS Power and Energy

As per Section IV, the BESS must meet the power and SoC constraints in (22).

Optimizing power allocation among battery clusters can disrupt balance, leading to unequal energy distribution and potential SoC limit breaches. When SoC limits are reached, the cluster's power is forced to zero, decreasing the objective function value. Therefore, the corresponding solution will be excluded during the iteration. This mechanism prevents declines in available BESS power due to energy imbalances.

C. Gradient-based Objective Function Optimization Algorithm

1) Conceptual Overview of Algorithm Construction

Heuristic algorithms often get trapped in local optima when dealing with high-dimensional optimization problems, leading to the curse of dimensionality. To address this, the gradient information of BESS loss model is used in this algorithm.

The algorithm iteratively corrects the initial variable I to $\bar{I}$, ensuring it meets specific criteria:

$$E(\bar{I}) > E(I) \tag{30}$$

Iterating the function sequence $I_{\mathcal{L}}(t)$ for $0 \leqslant t \leqslant T$, the maximum value of the objective function is obtained:

$$\lim_{\mathcal{L} \to \infty} E(I_{\mathcal{L}}) = \max_I E(I) \tag{31}$$

Therefore, the correction term ΔI of the current in each iteration must satisfy the relationship:

$$E(\bar{I}) - E(I) \approx E'(I)(\bar{I} - I) \triangleq E'(I)\, \Delta I \tag{32}$$

where $E'(I)$ is the Fréchet derivative of E with respect to I.

The BESS consist of m battery clusters, each requiring a current correction $\Delta I_j(t)$ over time t ($j = 1, 2, \cdots, m$; $0 \leqslant t \leqslant T$). After each iteration, $\Delta I_j(t)$ must satisfy specific conditions:

$$\sum_{j=1}^{m} \frac{\partial E}{\partial I_j} \Delta I_j > 0 \tag{33}$$

The algorithm aims to find $\Delta I_j(t)$ in each iteration that meets these conditions, gradually approaching the maximum value of E.

2) Model Gradient Calculation Method

The partial derivative of E with respect to the current $I_j(t)$ of battery cluster j is:

$$\frac{\partial E}{\partial I_j} \Delta I_j = \int_0^T I_j(t) V_{\mathrm{oc}}'(S_j) \frac{\partial S_j}{\partial I_j} \Delta I_j(t) \mathrm{d}t + \int_0^T \Delta I_j(t) V_{\mathrm{oc}}\left(S_j(t)\right) \mathrm{d}t \tag{34}$$

where S_j is the SoC of battery cluster j.

The SoC correction term is:

$$\frac{\partial S_j}{\partial I_j} \Delta I_j(t) = \frac{1}{C_{\mathrm{N}}} \int_0^t \Delta I_j(\tau)\, \mathrm{d}\tau \tag{35}$$

Substituting (35) into (34) yields:

$$\frac{\partial E}{\partial I_j} \Delta I_j = \frac{1}{C_{\mathrm{N}}} \int_0^T I_j(t) V_{\mathrm{oc}}'(S_j) \left(\int_0^t \Delta I_j(\tau) \mathrm{d}\tau \right) \mathrm{d}t + \int_0^T \Delta I_j(t) V_{\mathrm{oc}}\left(S_j(t)\right) \mathrm{d}t \tag{36}$$

Before each iteration, the parameters b_0, b_1, b_2, b_3, C_{N}, $I_j(t)$ are known at time t, allowing for the calculation of the partial derivative of the objective function.

3) Correction Amounts Constraints

a) Perturbation Relation: Battery Terminal Power Variation $\Delta P_{\mathrm{b}}(t)$ and Current Correction $\Delta I(t)$

$$\begin{aligned}&\Delta P_{\mathrm{b}}(t)=\\&\Delta I(t)V(S)+\frac{1}{C_{\mathrm{N}}}I(t,P_{\mathrm{b}})V'(S)\int_0^t\Delta I(\tau)\mathrm{d}\tau+\\&2I(t,P_{\mathrm{b}})\Delta I(t)R_{\Omega}+\frac{\Delta I(t)}{C_{\mathrm{P}}}\int_0^t I\left(\tau,P_{\mathrm{b}}\right)\mathrm{e}^{\frac{\tau-t}{R_{\mathrm{P}}C_{\mathrm{P}}}}\mathrm{d}\tau+\\&\frac{I(t,P_{\mathrm{b}})}{C_{\mathrm{p}}}\int_0^t\Delta I(\tau)\mathrm{e}^{\frac{\tau-t}{R_{\mathrm{P}}C_{\mathrm{P}}}}\mathrm{d}\tau\end{aligned}\tag{37}$$

Battery clusters are coupled through power. Establishing the $\Delta P_{\mathrm{b}}(t)$ and $\Delta I(t)$ relationship is essential to understand how current corrections are related across all clusters. The relationship between $\Delta P_{\mathrm{b}}(t)$ and $\Delta I(t)$ is given by (37), and the derivation process is detailed in Appendix B. In (37), all variables except for ΔP_{b} and ΔI are known state parameters at time *t*.

b) Relationship among Battery Clusters' Power Corrections

The relationship between the power correction on the battery side $\Delta P_{j,\mathrm{b}}(t)$ and the system side $\Delta P_j(t)$ for the *j*th battery cluster is given as:

$$\Delta P_{j,\mathrm{b}}(t)=\Delta P_j(t)\eta_{j,\mathrm{PCS}}\tag{38}$$

The sum of the power corrections $\Delta P_j(t)$ on the system side equals the total power correction ΔP is:

$$\Delta P(t)=\sum_{j=1}^{m}\Delta P_j(t)=\sum_{j=1}^{m}\frac{1}{\eta_{j,\mathrm{PCS}}}\Delta P_{j,\mathrm{b}}(t)\tag{39}$$

According to (28) and (29), the BESS must satisfy the power constraints. The total charging and discharging power of the BESS equals the total power demand $P_{\mathrm{sys}}(t)$, and the power of each battery cluster must not exceed the cluster's rated power P_{N}, i.e.:

$$\begin{cases}P(t)+\Delta P(t)=P_{\mathrm{sys}}(t)\\P_j(t)+\Delta P_j(t)<P_{\mathrm{N}}\end{cases}\tag{40}$$

In summary, the relationship between the power correction of each battery cluster is obtained as follows:

$$\begin{cases}\sum_{j=1}^{m}\frac{1}{\eta_{j,\mathrm{PCS}}}\Delta P_{j,\mathrm{b}}(t)=\Delta P(t)\\\frac{1}{\eta_{j,\mathrm{PCS}}}\Delta P_{j,\mathrm{b}}(t)<P_{\mathrm{N}}-P_j(t),\ (j=1,2,\cdots,m)\end{cases}\tag{41}$$

D. Power Allocation Coefficients Calculation Method

1) Unified Current Correction Iterative Discriminant for Dual Battery Clusters

a) Perturbation Relation in Discrete Time Domain: $\Delta P_{\mathrm{b}}(t)$ and ΔI(t)

Define the polynomials H_{α}, H_{β}, H_{γ} as shown in Appendix C. These polynomials, excluding the current corrections $\Delta I(t)$, can be considered as the state parameters of the *n*th iteration. Consequently, equation (37) can be reformulated for clearer observation, as:

$$\begin{aligned}\Delta P_{\mathrm{b}}(t)=H_{\alpha}(t)\Delta I(t)+H_{\beta}(t)\int_0^t\Delta I(\tau)\mathrm{d}\tau+\\H_{\gamma}(t)\int_0^t\Delta I(\tau)\mathrm{e}^{\frac{\tau-t}{R_{\mathrm{P}}C_{\mathrm{P}}}}\mathrm{d}\tau\end{aligned}\tag{42}$$

Discretizing the time domain with a time step $\Delta\tau=1$, equation (42) can be rearranged as follows:

$$\begin{aligned}\Delta P_{\mathrm{b}}(t)=\left[H_{\alpha}(t)+H_{\beta}(t)+H_{\gamma}(t)\right]\Delta I(t)+\\\sum_{\tau=1}^{t-1}\Delta I(\tau)\left(H_{\beta}(t)+H_{\gamma}(t)\mathrm{e}^{\frac{\tau-t}{R_{\mathrm{P}}C_{\mathrm{P}}}}\right)\end{aligned}\tag{43}$$

Define $H_{\Sigma}(t)$, $\theta(t)$, and $\varphi(\tau-t,\ t)$ as detailed in Appendix D, which do not contain $\Delta I(t)$ at time *t*, and considered as constants. Further rearranging (43) yields:

$$\Delta P_{\mathrm{b}}(t)=H_{\Omega}(t)\times\Delta I(t)+\theta(t)\tag{44}$$

b) Recursive Transformation of $\Delta I_1(t)$ and $\Delta I_2(t)$ for Dual Battery Clusters

According to the power correction constraints of (41), there are two battery clusters (*m*=2), the subscripts 1 and 2 of the variables correspond to battery clusters 1 and 2 respectively, and the corrections exhibit the following relationship:

$$\Delta P_{2,\mathrm{b}}(t)=-\frac{\eta_{2,\mathrm{PCS}}(t)}{\eta_{1,\mathrm{PCS}}(t)}\Delta P_{1,\mathrm{b}}(t)+\eta_{2,\mathrm{PCS}}(t)\Delta P(t)\tag{45}$$

Substituting (44) and expressing $\Delta I_2(t)$ in terms of $\Delta I_1(t)$:

$$\begin{aligned}\Delta I_2(t)=-\frac{H_{1,\Sigma}(t)}{H_{2,\Sigma}(t)}\frac{\eta_{2,\mathrm{PCS}}(t)}{\eta_{1,\mathrm{PCS}}(t)}\Delta I_1(t)-\frac{1}{H_{2,\Sigma}(t)}\theta_2(t)-\\\frac{1}{H_{2,\Sigma}(t)}\frac{\eta_{2,\mathrm{PCS}}(t)}{\eta_{1,\mathrm{PCS}}(t)}\theta_1(t)+\frac{\eta_{2,\mathrm{PCS}}(t)}{H_{2,\Sigma}(t)}\Delta P(t)\end{aligned}\tag{46}$$

Simplifying the coefficient for clarity, defined polynomials $\mu(t)$, $\varepsilon(t)$, $\nu(t)$, $\delta(t)$, as detailed in Appendix E, and (46) can be rewritten as:

$$\Delta I_2(t)=\mu(t)\Delta I_1(t)+\varepsilon(t)\theta_1(t)+\nu(t)\theta_2(t)+\delta(t)\tag{47}$$

On the right side of (47), only $\theta_1(t)$ contains $\Delta I_1(t)$. Substituting the expanded form of $\theta_1(t)$ yields:

$$\begin{aligned}\Delta I_2(t)=\underbrace{\mu(t)\Delta I_1(t)+\varepsilon(t)\theta_1(t)+\delta(t)}_{G[\Delta I_1(t)]}\cdots-\\\frac{1}{H_{\Sigma 2}(t)}\left\{\sum_{\tau=1}^{t-1}\Delta I_2(\tau)\varphi_2\left(\tau-t,t\right)\right\}\end{aligned}\tag{48}$$

Substitute recursively once:

$$\begin{aligned}\Delta I_2(t)=G\left[\Delta I_1(t)\right]-\frac{1}{H_{2,\Sigma}(t)}\left\{\sum_{\tau=1}^{t-1}\left[G\left(\Delta I_1(\tau)\right)\cdots-\right.\right.\\\left.\left.\frac{1}{H_{2,\Sigma}(\tau)}\left(\sum_{\rho=1}^{\tau-1}\Delta I_2(\rho)\varphi_2(\rho-\tau,\tau)\right)\right]\varphi_2(\tau-t,t)\right\}\end{aligned}\tag{49}$$

The relationship pattern between ΔI_2 and ΔI_1 is:

$$\Delta I_2(t) = F\left[\Delta I_1(t), \Delta I_2(t-1), \cdots, \Delta I_2(1), t\right] \quad (50)$$

where $F[\cdot]$ is relation operator between ΔI_1 and ΔI_2.

Equation (50) shows that $\Delta I_2(t)$ can be expressed using $\Delta I_1(t)$ and the ΔI_2 sequence over time range [1, t−1]. If (50) is recursively iterated, the time step of ΔI_2 can be gradually reduced. Through multiple recursive substitutions, $\Delta I_2(t)$ can be expressed by $\Delta I_1(\tau)$ (τ=1, 2,⋯, t):

$$\Delta I_2(t) = F\left[\Delta I_1(1), \Delta I_1(2), \cdots, \Delta I_1(t), t\right] \quad (51)$$

According to (D2) in Appendix D, the terms in (51) decrease as τ approaches 1 due to the RC time constant. Therefore, only the terms near t need to be retained based on the precision requirements.

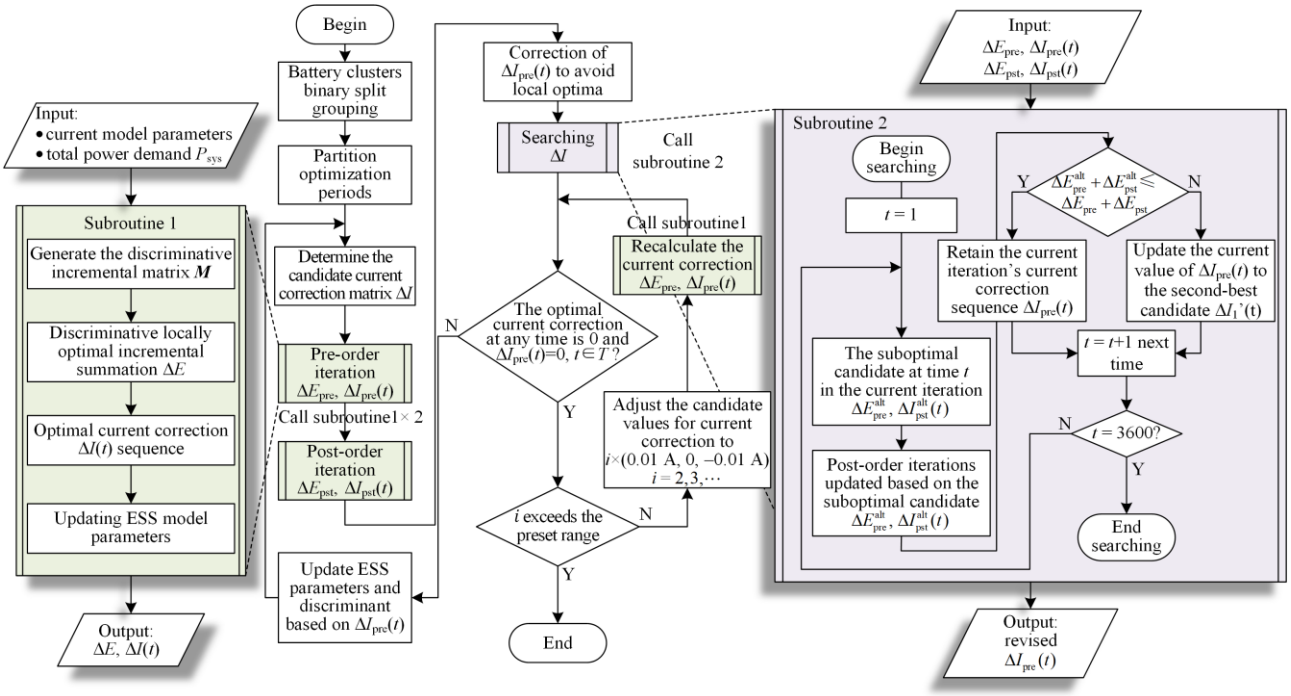

Fig. 10. Flowchart of iterative process for the current correction $\Delta I(t)$.

c) Iterative Discriminant: Gradient-based Iterative Discriminant

The iterative discriminant for dual battery clusters is given as:

$$\frac{\partial E}{\partial I_1}\Delta I_1 + \frac{\partial E}{\partial I_2}\Delta I_2 > 0 \quad (52)$$

All expressions involving ΔI_2 are converted to terms of ΔI_1, and are then discretized in time domain. The iterative discriminant for the correction $\Delta I_1(t)$ in a dual clusters system (m=2) can be obtained as:

$$\begin{aligned}&\frac{\partial E}{\partial I_1}\Delta I_1 + \frac{\partial E}{\partial I_2}\Delta I_2 = \sum_{t=1}^{T}\Delta I_1(t)V_{\text{oc}}(S_1) + \\ &\frac{1}{C_N}\sum_{t=1}^{T}\left\{I_1(t)V'_{\text{oc}}(S_1)\sum_{s=1}^{t}\Delta I_1(t)\right\} + \\ &\frac{1}{C_N}\sum_{t=1}^{T}\left\{I_2(t)V'_{\text{oc}}(S_2)\sum_{\tau=1}^{t}F\left[\Delta I_1(1),\cdots,\Delta I_1(\tau),\tau\right]\right\} + \\ &\sum_{t=1}^{T}F\left[\Delta I_1(1),\cdots,\Delta I_1(t),t\right]V_{\text{oc}}(S_2) > 0\end{aligned} \quad (53)$$

During the iterative solving of $\Delta I_1(t)$, if the iterative discriminant holds, it indicates that the current iteration is converging towards the extremum of the objective function. This criterion is the key formula for enhancing the computational efficiency of the algorithm.

2) Iterative Solution for Current Correction $\Delta I(t)$

The optimization of $\Delta I_1(t)$ is not a unique solution problem. This section proposes an iterative method for solving the $\Delta I_1(t)$ sequence.

a) Preprocessing: Partitioning Optimization Periods

To improve computational efficiency, the time domain is divided into intervals. Considering that the battery's RC time constant is on the order of minutes and the SoC cycle spans 24 hours, a 1-hour optimization interval is deemed to be appropriate based on repeated trials.

Model parameters are updated only after determining the $\Delta I_1(t)$ sequence and before the next iteration. This means the $\Delta I_1(t)$ sequence has no temporal correlation, allowing values to be searched in any order, thereby enhancing search efficiency.

b) Main Program

The workflow for iterative calculation of current correction sequence is shown in Fig. 10. Additionally, it needs to satisfy the following rules.

1) $\Delta I_1(t)$ can be a small constant, i.e., –0.01 A, 0 A, 0.01 A, chosen to control data granularity and prevent excessive overcorrection.

2) To prevent local optima, multiple initial $\Delta I_1(t)$ sequences are used (30 in this case).

3) The power correction amount $\Delta P_b(t)$ corresponding to $\Delta I_1(t)$ must satisfy the power constraint in (41).

4) The initial value of the first current correction corresponds to the average power allocation mode, all power clusters' allocation coefficient $k = 0.01$.

c) Call Subroutine 1: Preorder Iteration

1) Calculate the increments of the discriminant (53) for each candidate value (–0.01, 0, 0.01) at each time point. Form an increment matrix $\boldsymbol{M}_{\text{pre}}$ with these values, resulting in a 3×3600 matrix.

2) The maximum element in t column of $\boldsymbol{M}_{\text{pre}}$ represents the local optimal increment at time t. Summing these values across all time yields ΔE_{pre}.

3) The optimal current corrections at each time point corresponding to ΔE_{pre} are denoted as $\Delta I_{\text{pre}}(t)$.

4) Update the model and the discriminant (53) based on ΔI_1.

d) Recall Subroutine 1: Postorder Iteration

Similar procedure, calculate the postorder iteration's increment matrix $\boldsymbol{M}_{\text{pst}}$, local optimal increment ΔE_{pst}, and current correction $\Delta I_{\text{pst}}(t)$.

e) Call Subroutine 2: Correction of $\Delta I_{\text{pre}}(t)$ for Avoiding Local Optima

Due to the multi-peak, multimodal nature, multiple local optima are possible. Subroutine 2 provides a mechanism to avoid local optima:

1) Change $\Delta I_{\text{pre}}(t)$ by selecting a "suboptimal alternative value," blend it with other current corrections at other times to form a new correction sequence $\Delta I_{\text{pre}}^{\text{alt}}(t)$, then update the objective function increment $\Delta E_{\text{pre}}^{\text{alt}}(t)$.

2) Recalculate $\Delta E_{\text{pst}}^{\text{alt}}$ during the second iteration.

3) If $\Delta E_{\text{pre}}^{\text{alt}} + \Delta E_{\text{pst}}^{\text{alt}} \leqslant \Delta E_{\text{pre}} + \Delta E_{\text{pst}}$, then retain the optimal candidate value of $\Delta I_{\text{pre}}(t)$ from step a).3).

4) if $\Delta E_{\text{pre}}^{\text{alt}} + \Delta E_{\text{pst}}^{\text{alt}} > \Delta E_{\text{pre}} + \Delta E_{\text{pst}}$, update the value of $\Delta I_{\text{pre}}(t)$ to the suboptimal alternative value.

5) Check all ΔI_{pre} at 3600 time points by method above, obtain new ΔI_{pre} sequence, update the model and discriminant (53) for the next iteration.

f) Exit Iteration Condition

1) Repeat the above steps until $\Delta I_{\text{pre}}(t) = 0$ $(t \in T)$ for all time. Then, adjust current correction candidate to [$i \times 0.01$ A, 0, $-i \times 0.01$ A] and go back to Step c). Based on debugging experience, selecting i=[2,3,4,5] is appropriate.

2) If for all i=2, 3…, condition $\Delta I_{\text{pre}}(t) = 0$ $(t \in T)$ still holds, terminate the iteration.

3) If any i=2, 3…, results in $\Delta I_{\text{pre}}(t) \neq 0$, update the model and the iterative discriminant (53), and repeat from Step c).

The sum of all $\Delta I_{\text{pre}}(t)$ from the iterations will be the total current correction, denoted as $\Delta I_1(t)$.

g) Ending Program

Compute the $\Delta I_2(t)$ sequence using $\Delta I_1(t)$ according to (49).

Method enhances the search efficiency by local negative gradient directionality, without using random search mechanisms in heuristic algorithms. However, its effectiveness in avoiding local optima over extended optimization periods is still limited.

3) Binary-split-grouping for Muti-cluster's Power Allocation Coefficient

After obtaining $\Delta I_1(t)$ and $\Delta I_2(t)$, power corrections $\Delta P_1(t)$ and $\Delta P_2(t)$ can be obtained by (37) and (B1). Therefore, the allocation coefficients $\boldsymbol{K}$ for a dual-battery cluster system can be obtained by (19).

The above method can be combined with the binary-split-grouping approach to calculate the power allocation coefficients for BESS with more than two battery clusters. With multiple battery clusters ($m > 2$), allocation coefficients are hierarchically calculated using a splitting method. First, clusters are divided into two groups, each group with approximately equal numbers. For instance, for a system with 7 battery clusters, they can be divided into two groups: one with 4 clusters and the other with 3 clusters. Then, each group undergoes further binary splitting, continuing until each group contains less than one battery cluster. This grouping process is illustrated in Fig. 11.

As shown in Fig. 11, the allocation coefficient calculation process using binary-split-grouping is illustrated for a BESS with 100 battery clusters, corresponding to the case in Section V. It undergoes 7 levels of binary splitting to generate 128 allocation coefficients. When allocation coefficients exceed 100, the total actual power of all battery clusters will fall short of the system's total power. This is because each cluster's power must lie within [0, P_N], any coefficients failing to meet the power constraint will lead to lower battery energy than if the constraint were satisfied. During iteration, such coefficients sets will not yield optimal fitness in the objective function, and allocation coefficients that do not correspond to actual battery clusters will be set to zero. A total of 28 empty allocation coefficient vectors are discarded, obtaining 100 valid allocation coefficients.

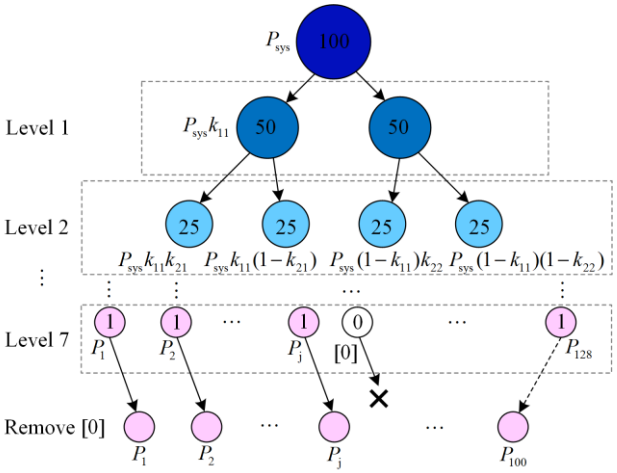

Fig. 11. Calculation of power allocation coefficients by binary split grouping.

V. Case Study

A. Test System and Settings

1) BESS Parameters

A 5 MW / 20 MWh BESS model is constructed using Simulink/Simscape. Figure 12 shows the circuit structure and key simulation sub models.

Lithium battery cell circuit model parameters are based on measured data of Shenhang LR12500SA lithium batteries: $R_\Omega = 0.0232\ \Omega$, $R_p = 0.0185\ \Omega$, $C_p = 12091$ F, and the open-circuit voltage V_{oc} is determined by (5). Capacity for a single cell is 12.5 Ah. A battery module consists of 24 cells in parallel, and 200 groups in series. A battery management system controls cells to maintain ideal SoC and voltage balance.

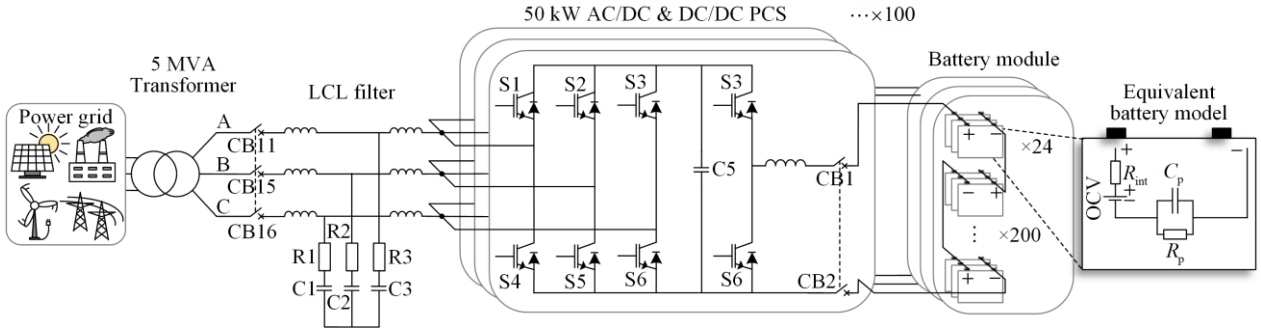

Fig. 12. BESS circuit structure & simulation model.

The module is connected to the low-voltage side of the 50 kW DC/DC PCS, which is then connected to the DC side of the AC/DC with constant voltage of 700 V, forming a battery cluster rated at 50 kW/200 kWh. The AC sides of 100 clusters are parallel connected to a 5 MVA transformer, consisting of the complete 5 MW/20 MWh BESS.

2) Basic Information of Load

Using historical load of a regional power system as the original data, a simulated load time series, with a 5-minute forecasting precision, is generated for peak-shaving. Key data of the load is shown in Table II.

TABLE II
Main Indicators Overview of Power Load

Items	Value (MW)	Date (day)
Min. annual load	134.0	51
Max. annual load	234.0	328
Min. peak-valley diff	24.5	266
Max. peak-valley diff	53.0	327

B. Typical Day Sample Case

1) Comparison of Energy Losses for Each Component

a) Balanced Mode

As a control group, Table III shows the detailed data on losses and efficiency under balanced mode, where E_{bat_ss} and E_{bat_ts} is the integral energy corresponding to P_{bat_ss} and P_{bat_ts}.

TABLE III
Loss and Efficiency Under Balanced Mode (1 Day)

Items	Energy loss (kWh)	Proportion (%)	Average power efficiency (%)
1 Transformer	135.54	3.21	99.53
2 AC/DC	1062.76	25.18	96.38
3 DC/DC	1880.53	44.56	93.66
4 BAT	1141.71	27.05	96.09
4-1 E_{bat_ss}	1154.90	27.36	
4-2 E_{bat_ts}	−13.19	−0.31	
Total	4220.53	100.00	86.33

b) Optimized Mode

After optimization, the energy losses, the proportion of total losses, the average power efficiency of each BESS component, and their changes are shown in Table IV.

Compared to the balanced mode in Table III, the total ESS losses decrease by 130.9 kWh, and the average power efficiency increases by 0.46%. The most significant contribution comes from PCS, as it accounts for the largest proportion of the total losses.

TABLE IV
LOSS AND EFFICIENCY UNDER OPTIMAL MODE (1 DAY)

Items	Energy loss (kWh)		Proportion (%)		Average power efficiency (%)	
	Value	Change	Value	Change	Value	Change
1 Transformer	135.74	+0.20	3.32	+0.11	99.53	0.00
2 AC/DC	1014.03	–48.73	24.80	–0.39	96.56	+0.18
3 DC/DC	1792.43	–88.10	43.83	–0.73	93.98	+0.32
4 BAT	1147.43	+5.73	28.05	+1.00	96.09	0.00
4-1 E_{bat_ss}	1162.38	+7.49	28.42	+1.06		
4-2 E_{bat_ts}	–14.95	–1.76	–0.37	–0.05		
Total	4089.64	–130.90	100.0	0.00	86.79	+0.46

2) Time Series Data Presentation

Key data time series curves reveal the detailed actions of the optimization strategy. BESS power allocation coefficients heatmap, charge/discharge power, SoC, and instantaneous power efficiency are shown in Fig. 13.

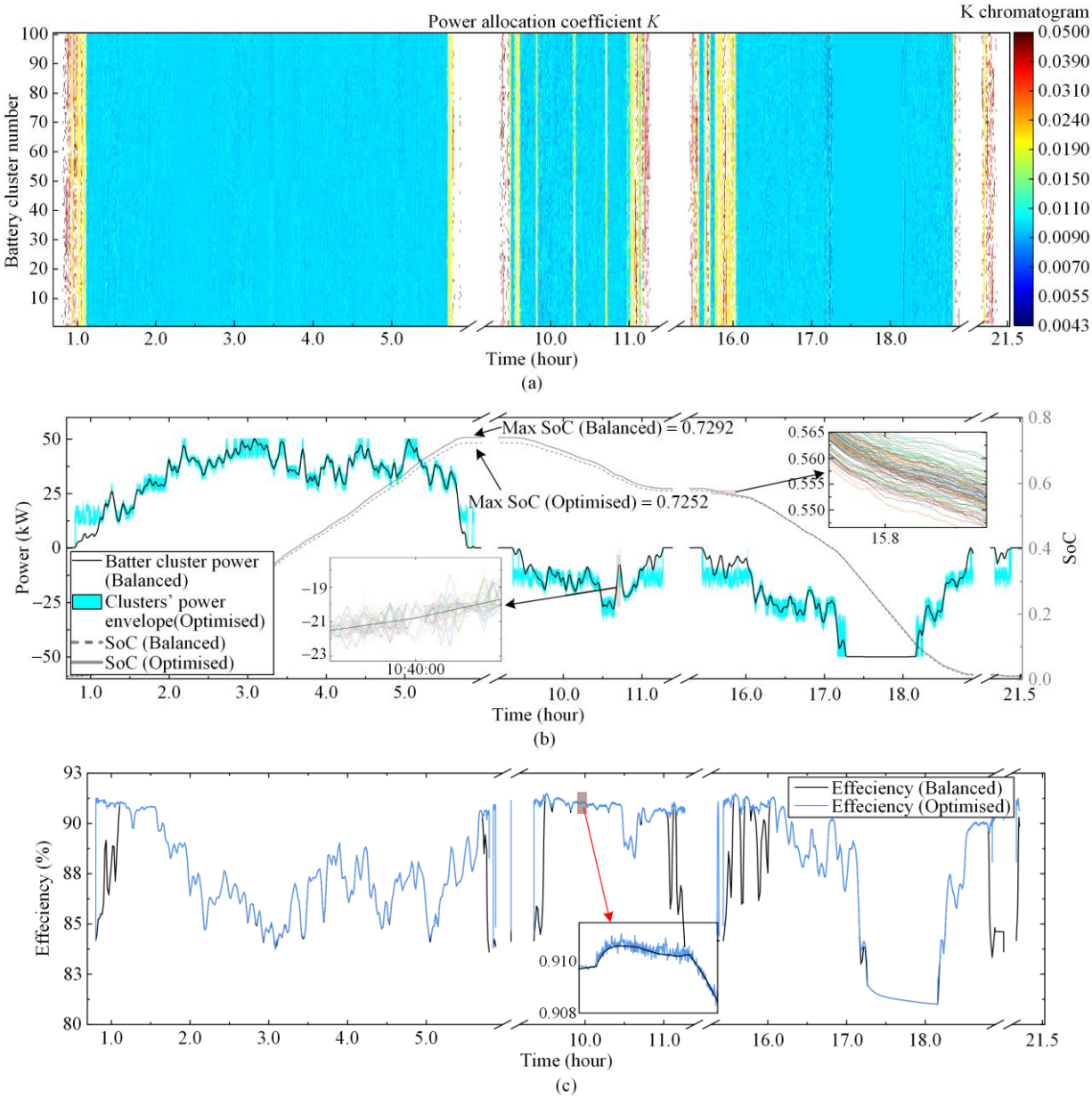

Fig. 13. Key data of BESS operation. (a) Power allocation coefficient *k*. (b) Charging/discharging power & SoC of battery clusters. (c) Power efficiency.

a) Power Allocation Coefficients

Figure 13(a) shows the power allocation coefficients in a heatmap, revealing an unbalanced power distribution among the battery clusters. The time granularity of the data is 1 . The horizontal axis corresponds to time, while the vertical axis corresponds to the battery cluster numbers in the BESS. The different colors correspond to different k values. The mapping relationship is shown in the color bar on the right side. When the battery cluster power is evenly allocated, indicated by $k = 0.01$ and shown in light blue. Except for the period between 17:30–18:30, the BESS is charged at full power and is forced into balanced allocation. At all other times, the power allocation is unbalanced.

b) Charge/Discharge Power, Energy, and SoC

In Fig. 13(b), the black line is the battery cluster power in balanced mode, while the cyan envelope is the power distribution range of the 100 battery clusters in optimized mode. The enlarged view shows the power detail of all clusters. The total charging energy remains unchanged after optimization, but improved system efficiency allows the BESS to discharge more energy. Table V shows the optimization effect.

TABLE V
ESS ENERGY AND EFFICIENCY CHANGE (1 DAY)

Items	Balanced mode	Optimised mode	Change
Maximum SoC	0.7252	0.7292	0.004 (+0.55%)
Total charging energy (kWh)	16574	16574	0
Total discharging energy (kWh)	12354	12485	131 (+1.06%)
Round-trip efficiency (%)	74.54	75.33	+0.79

c) Instantaneous Power Efficiency

Figure 13(c) shows the instantaneous power efficiency differences before and after optimization. For the total 10.53 hours operation, during 6.17 hours, the post-optimization efficiency is higher, with over 1% increase for 1.22 hours, whereas during 3.46 hours, the post-optimization efficiency is lower, but the difference is under 0.1%. The enlarged view highlights post-optimization efficiency decrease, indicating that the algorithm targets global optimization, while BESS as a time-varying system, the global optimum does not mean optimum at every moment.

3) Energy Loss Analysis

a) Analysis of Non-Storage Component Losses

Figure 13(b) shows power distribution changes among battery clusters, statistics are shown in in Table VI.

After optimization, average power for each battery cluster increases by 11.9%–13.2%, and time operating at loads <10 kW decreases by 89.1%–93.7%. Thus, light-load operating is alleviated, and the maximum difference in SoC between the most imbalanced clusters is 0.012. That indicates energy imbalance among clusters is negligible.

TABLE VI
POWER CUMULATIVE TIME DISTRIBUTION CHANGE (1 DAY)

Items	Balanced mode	Optimised mode	Percentage difference (%)
Average power (kW)	27.20	[30.45, 30.78]	[+11.9, +13.2]
<10kW runtime (hour)	1.87	[0.10, 0.18]	[–90.4, –94.7]
Total runtime (hour)	10.68	[9.44, 9.55]	[–11.6, –10.6]
<10kW/total runtime (%)	17.5	[1.1, 1.9]	[–89.1, –93.7]

b) Analysis of Energy Storage Component Losses

Figure 14 compares the battery cell currents (I and I_c) before and after optimization. The envelopes of I and I_c under optimal mode align around the original balanced mode curve. The optimized I and I_c curves are shown in the enlarged view.

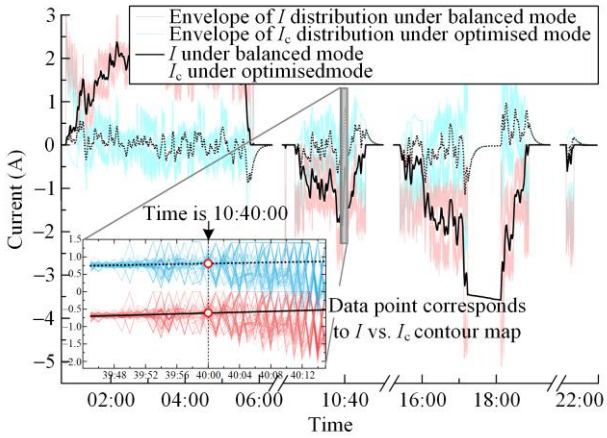

Fig. 14. Battery I & I_c time series under different modes.

Figure 15 shows a scatter plot of I vs. I_c distribution at 10:40:00, along with the current- P_{bat_ts} gradient field. Figure 8(b) presents the complete current range across four quadrants for the P_{bat_ts} gradient field, while the gradient field in Fig. 15 focuses on a local magnification near the current operating point at the specific moment.

In Fig. 15, the contour lines in the P_{bat_ts} gradient field represent the magnitude of the P_{bat_ts} component corresponding to different I and I_c values. It can be observed that the overall trend of P_{bat_ts} decreases from the lower-right corner to the upper-left corner.

In optimized mode (blue point), due to the unbalanced allocation strategy, the current operating points of the 100 battery clusters no longer coincide, and spread across different gradient directions compared to the balanced mode (red point).

Since the power allocation strategy only changes the individual power of the battery clusters while maintaining the total power, it means that in optimized mode (blue point), the increase in power at some operating

points in the $P_{\text{bat\_ts}}$ gradient field is offset by the decrease in power at others. Figure 15 illustrates a pair of complementary battery clusters (No. 1 & No. 2), where the sum of their energy changes is nearly zero. The operating point of No. 1 has dropped about 6 contour levels relative to the balanced mode operating point (red point in the middle), while No. 2 has risen by about 1 contour level. This indicates that the redistribution of power results in an overall decrease in $P_{\text{bat\_ts}}$ for this pair of complementary battery clusters at this moment. The corresponding changes in the $P_{\text{bat\_ts}}$ component are recorded in Table VII.

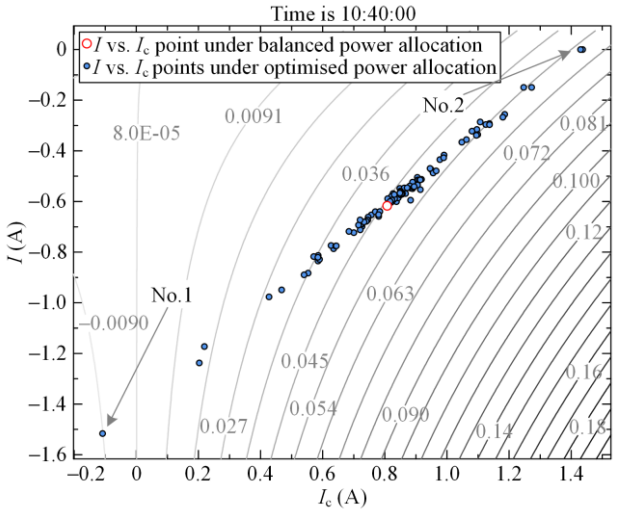

Fig. 15. Scatter plot of I vs. I_c for each battery cluster at 10:40:00.

The decrease in Cluster 1 on the contour is greater than the increase in Cluster 2, leading to a net decrease of 0.045 W for this pair of battery cells. As mentioned earlier, each battery cluster contains 200×24 battery cells, and the SoC is balanced among individual cells. Therefore, the total decrease in $P_{\text{bat\_ts}}$ for this complementary cluster is 216 W, representing the total change in $P_{\text{bat\_ts}}$ for battery clusters No. 1 and No. 2 at the single time point of 10:40:00.

Based on this mechanism, considering that the total power across all battery clusters remains unchanged, the 100 battery clusters can be treated as a whole, forming a power-complementary group. This results in a total $E_{\text{bat\_ts}}$ decrease of 1.76 kWh over 24 hours. Similarly, $E_{\text{bat\_ss}}$ increases by 7.49 kWh, as shown in Table IV.

TABLE VII
$P_{\text{bat\_ts}}$ OF COMPLEMENTARY BATTERY CELLS
(W)

Items	Balanced mode	Optimised mode	Difference	Percentage difference
Cluster No.1	0.0452	−0.0090	−0.0542	−119.9%
Cluster No.2	0.0452	0.0544	+0.0092	+20.4%
Total	0.0904	0.0454	−0.0450	−49.8%

4) Optimization Algorithm Performance Analysis

This section uses particle swarm optimization (PSO) as a comparing group to analyze algorithm performance. As shown in Fig. 7, time-varying optimization requires preserving temporal correlations among parameters, ideally optimizing allocation coefficients collectively. Due to PSO's inefficiency with large arrays, we segment the 24 hour optimization into 30 s intervals, each particle $\boldsymbol{K}_{(1\times30)}$ contains 30 allocation coefficients. Excluding non-operating times, there are 10.68 hours, resulting in 1282 groups. A global search follows the segmented search to incorporate inter-group correlations.

To balance performance and computation time, the particle count is set to 10. The allocation coefficients in balanced mode and battery energy increment are used as the initial particle values and fitness values. The maximum number of iterations is 25.

The position update equation is given as:

$$k_{i+1} = k_i + \mathrm{w}v_i + \mathrm{c}_1 r_1 (k_{\mathrm{m}} - k_i) + \mathrm{c}_2 r_2 (k_{\mathrm{m\_glb}} - k_i) \quad (54)$$

where the inertia weight w=0.85; cognitive learning factor $\mathrm{c}_1 = 0.5$; and social learning factor $\mathrm{c}_2 = 0.45$; k_{m} represents each particle's historical best value; $k_{\mathrm{m\_glb}}$ is the global best value; k_i is the particle at iteration i, each particle is limited within the allocation coefficient range $k_i \in [0,1]$, and the initial value of k corresponds to the balanced allocation mode, i.e., $k_1 = 0.01$; and the update velocity is constrained to $v_i \in [-1,1]$; r_1 and r_1 are mean random perturbation between (0,1).

The fitness f is computed by referencing a Simscape model. To minimize iteration time, "fast restart", "load initial state", "save final state" parameters are used, along with Parsim for parallel simulations to further reduce Simscape computation time. The allocation coefficient k_{i+1} obtained from each PSO iteration is input into the Simscape model, which returns the real-time battery energy E, thus updating the fitness f.

To compare algorithm performance, PSO and the optimised algorithm are run on the same computer, and their performances are compared in Table VIII.

TABLE VIII
ALGORITHMS PERFORMANCE COMPARISON (1 DAY)

items	PSO	Optimised algorithm
Number of subgroups	1282 (30 s/grp)	11 (3600 s/grp)
Iteration limit per group	25	3000
Total number of iterations	32050	33000
Average iteration time (s)	3.41	0.26
Max. iteration time (s)	3.62	0.31
Min. iteration time (s)	3.28	0.20
Total iteration time (hour)	30.36	2.38
Energy loss (kWh)	4091.45	4089.64

As shown in Table VIII, due to enhanced multivariable processing capability, the proposed method extends each grouping period from 30 s to 3600 s. Consequently, the 10.68 hours of non-zero power in 1 day can now be divided into 11 groups for optimization, greatly reducing group numbers. The maximum iterations per group are also raised to 3000. The average iteration time of PSO is 13 times longer than the proposed method, as PSO involves the Simscape model in each iteration, slowing fitness updates. In contrast, the proposed time-varying optimization leverages a model gradient criterion (53) to expedite iteration. For a typical 1-day case, PSO exceeds 24 hours, implying that PSO would require at least 30.36 hours lead time to complete a 24-hour power allocation plan. Thus, PSO encounters application challenges in time-varying optimization.

To compare the iteration details of the two method, the 01:00–02:00 period in this case is used as a sample. Figure 16 illustrates the trend of fitness increment (i.e., battery energy increment ΔE) with respect to iteration count and simulation time. In Fig. 16, the blue fitness curve of the PSO within the 01:00–02:00 optimization interval is assembled from 120 sub-intervals, totaling 3000 iterations, while the red curve representing the proposed method uses only a single interval, also set to 3000 iterations.

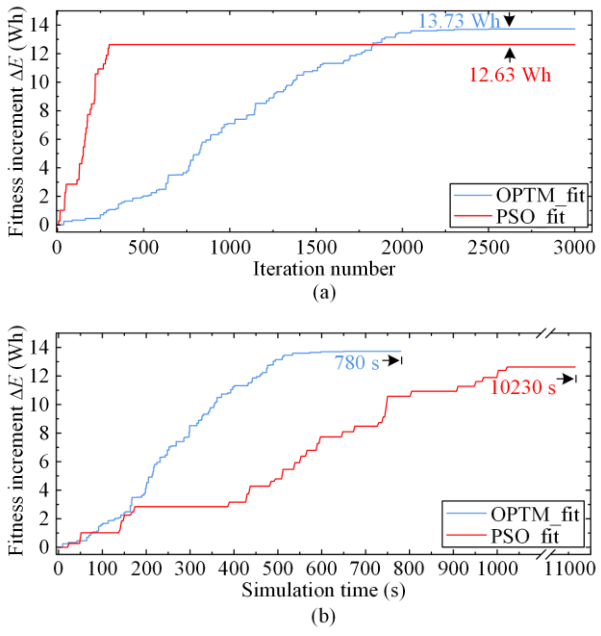

Fig. 16. Fitness increment. (a) Over iterations. (b) Over time.

As shown in Fig. 16(a), within the sample interval, PSO converges around the 300th iteration. In contrast, the proposed method reaches a better result after approximately 2500 iterations, achieving a final convergence value which is 13.73–12.63 = 1.1 (Wh) higher than PSO. This suggests that PSO falls into a local optimum within this interval. As shown in Fig. 16(b), in terms of simulation time, each iteration of PSO takes longer. Thus, despite the higher iteration count in the proposed method, the actual time taken is 10230–781 = 9449 (s) less than PSO.

In summary, the proposed algorithm achieves shorter iteration time, manages more variables, and optimizes longer intervals per iteration, ensuring temporal consistency in time-varying optimization.

C. Annual Sample Case

1) Comparison of Energy Losses for Each Component

a) Balanced Mode

As a control, this case calculated detailed BESS losses under balanced mode with a 5 MW peak-shaving depth, as shown in Table IX.

TABLE IX
LOSS AND EFFICIENCY UNDER BALANCED MODE (365 DAYS)

Items	Energy loss (MWh)	Proportion (%)	Average power efficiency (%)
1 Transformer	23.03	2.98	99.58
2 AC/DC	201.30	26.05	96.38
3 DC/DC	336.18	43.50	94.00
4 BAT	212.26	27.47	96.16
4-1 E_{bat_ss}	219.82	28.45	
4-2 E_{bat_ts}	–7.56	–0.98	
Total	772.77	100.00	86.76

In BESS losses, PCSs account for 69.55%, batteries for 27.47%, and transformer for only 2.98%. Thus, improving BESS efficiency mainly relies on enhancing PCS and battery efficiencies.

b) Optimized Mode

The detailed component losses in the optimized BESS are shown in Table X.

TABLE X
LOSS AND EFFICIENCY UNDER OPTIMAL MODE (365 DAYS)

Items	Energy loss (MWh)		Proportion (%)		Average power efficiency (%)	
	Value	Change	Value	Change	Value	Change
1 Transformer	23.23	+0.20	3.08	+0.10	99.58	0.00
2 AC/DC	194.78	–6.52	25.83	–0.22	96.51	+0.13
3 DC/DC	323.61	–12.57	42.91	–0.60	94.24	+0.24
4 BAT	212.58	+0.32	28.19	+0.72	96.17	+0.01
4-1 E_{bat_ss}	221.17	+1.35	29.33	+0.88		
4-2 E_{bat_ts}	–8.59	–1.03	–1.14	–0.16		
Total	754.21	–18.56	100.0	0.00	87.10	+0.34

Based on Tables IX and X, Fig. 17 shows the cumulative bar chart of components losses.

The total charge/discharge energy and the round-trip efficiency over a year are shown in Table XI.

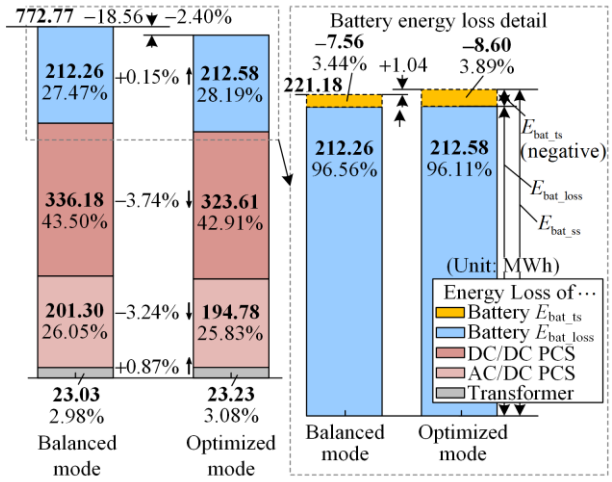

Fig. 17. Components loss proportion.

TABLE XI
ESS ENERGY AND EFFICIENCY CHANGE (365 DAYS)

Items	Balanced mode	Optimised mode	Change
Total charge energy (MWh)	3125.12	3124.10	−1.02 (−0.03%)
Total discharge energy (MWh)	2352.35	2369.89	+17.54 (+0.75%)
Round-trip efficiency (%)	75.27	75.86	+0.59

2) Energy Loss Analysis

a) Analysis of Non-storage Component Losses

This section compares the cumulative time distribution of absolute battery cluster power before and after optimization shown in Fig. 18.

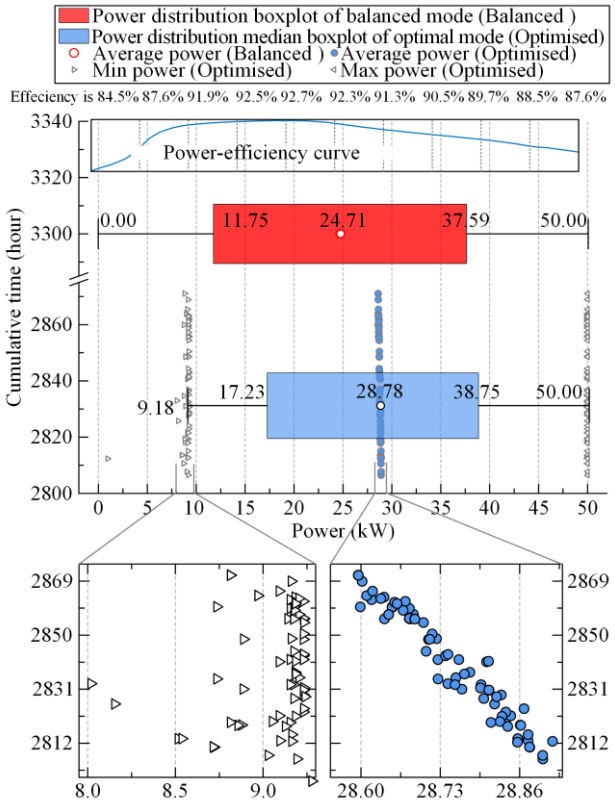

Fig. 18. Cumulative time distribution boxplot comparison.

In balanced mode, the power distribution among battery clusters is identical, so there is only one boxplot (red). In optimized mode, the power distribution varies among clusters, but plotting 100 boxplots is impractical. Figure 18 shows the average, maximum, and minimum power data points for each cluster, along with a boxplot of their median values (blue). The vertical axis corresponds to the median of the power cumulative time. Efficiency curve maps power-efficiency relationship.

Table XII compares some key power distribution data between the two modes.

TABLE XII
KEY STATISTICS FOR THE CUMULATIVE TIME DISTRIBUTION OF BATTERY CLUSTER POWER

Items	Balanced mode	Optimised mode (median boxplot)	Percentage difference (%)
Average power (kW)	24.71	28.78	+16.47
Minimum power (kW)	0.02	9.18	
<10 kW runtime (hours)	556	44	−92.17
<10 kW/total runtime (%)	20.23	1.24	−93.87
15–25 kW runtime (hours)	573	709	+23.73
15–25 kW/total runtime (%)	14.70	20.42	+38.91

The proportion of time with battery cluster power <10 kW is decreased by 93.87%, with power between 15–25 kW increased by 38.91%. That indicates light-load condition has been alleviated, while time operating within the high-efficiency range has been increased. These changes reduce overall losses in the BESS's non-storage components.

b) Analysis of Energy Storage Component Losses

The left inset of Fig. 19 shows the annual cumulative joint distribution 3D surface of battery cell currents I vs. I_c in balanced mode. In Fig. 19(a) is its projection heatmap on I vs I_c plane. With similar method, the current distribution heatmap for each battery cluster under optimized mode is shown in Fig. 19(b), with battery cluster No. 50 as an example.

Based on Section III, the heatmap is divided into 4 quadrants, and the average points of I and I_c are plotted, with balanced mode in red hollow and optimized mode in blue solid. Due to the nonlinear and non-additive relationship between current and power loss, these average points do not correspond to actual losses but serve to gauge relative trend changes across distributions.

The shift of current distribution under the optimized mode relative to the balanced mode can be observed from Fig. 20, where the arrows indicate the negative gradient direction. In Fig. 20, the overall shift trend aligns with the negative gradient direction, moving towards the reduction of P_{bat_ts}.

The data correspond with Table X, confirming that the proposed strategy can reduce battery losses by optimizing the current distribution.

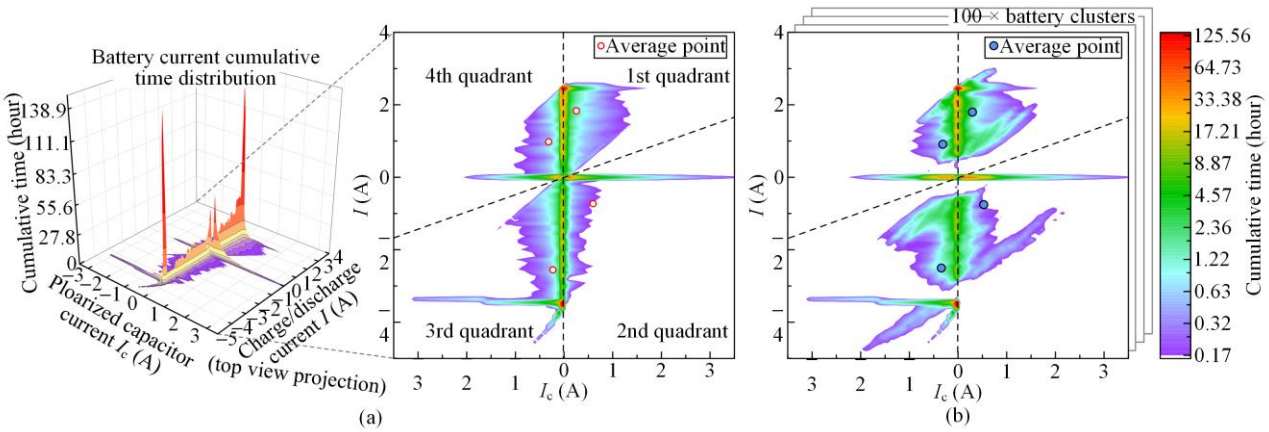

Fig. 19. Current cumulative time distribution of No.50 battery cluster. (a) Balanced power allocation. (b) Optimal power allocation.

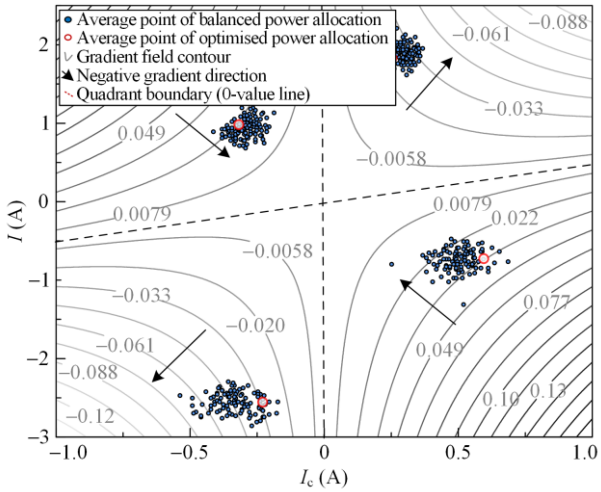

Fig. 20. I vs. I_c distribution average point under balanced/optimised strategy with P_{bat_ts} gradient field.

P_{bat_ss} is only related to I, so the I_c axis is disregarded. In Fig. 21, compared to the balanced mode, the current distribution slightly shifts towards the direction of increasing I, aligning with Table X, which shows a small increase in the steady-state component.

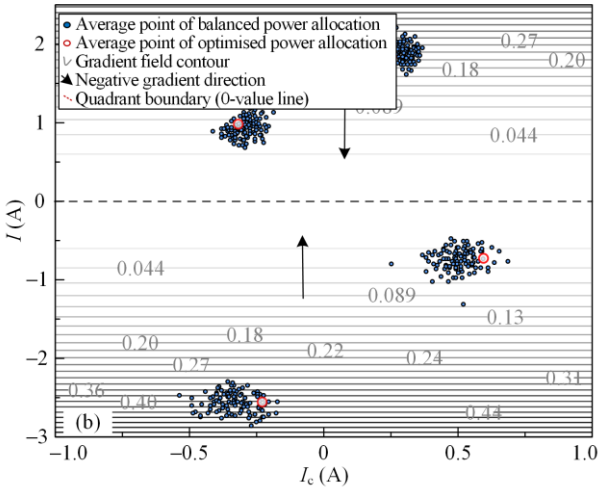

Fig. 21. I vs. I_c distribution average point under balanced/optimised strategy with P_{bat_ss} gradient field.

VI. Conclusion

This study analyzes the time-varying characteristics of BESS components and proposes loss optimization paths for non-storage and storage components based on model gradients. An optimization strategy for battery cluster power allocation considering time-varying characteristics is designed and validated through simulation. First, the load-rate vs. equivalent-efficiency curve curve is used to analyze BESS power distribution and evaluate the strategy's ability to reduce light-load operation, thereby lowering losses in time-invariant components. Second, the current vs. power loss component gradient fields are used to analyze battery current distribution, evaluating how the strategy-induced current distribution change leads to increased steady-state losses and decreased transient losses. It validates that time-varying optimization improves battery efficiency. Then, based on load data from a regional grid peak shaving scenario, a BESS simulation model is developed to calculate the loss composition and proportion for each component. Finally, after optimization, the total annual BESS losses are decreased by 2.40%, and the round-trip efficiency is improved by 0.59%.

In future research, it is essential to study the impact of different power demand characteristics on BESS losses, especially in high-penetration clean energy systems.

Appendix A

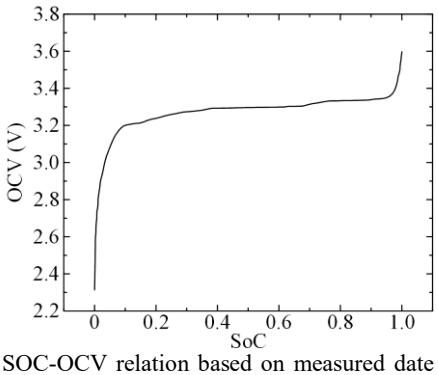

Fig. A1. SOC-OCV relation based on measured date of Shenhang LR12500SA lithium battery.

APPENDIX B

According to (25), the power and current constraint equations for the battery clusters are:

$$P_{\mathrm{b}}(t) \triangleq P_{\mathrm{sys}}(t) \times k \times \eta_{\mathrm{pcs}}(P) \tag{B1}$$

Substituting the power correction term into (25) yields:

$$P_{\mathrm{b}}(t)+\lambda\Delta P_{\mathrm{b}}(t)=I(t,P_{\mathrm{b}}+\lambda\Delta P_{\mathrm{b}})\times \left[\begin{array}{l} V\left(\dfrac{1}{C_{\mathrm{N}}}\displaystyle\int_0^t I(\tau,P_{\mathrm{b}}+\lambda\Delta P_{\mathrm{b}})\mathrm{d}\tau\right)\cdots+ \\ I(t,P_{\mathrm{b}}+\lambda\Delta P_{\mathrm{b}})R_{\mathrm{l}}+\dfrac{1}{C}\displaystyle\int_0^t I(\tau,P_{\mathrm{b}}+\lambda\Delta P_{\mathrm{b}})\mathrm{e}^{\frac{\tau-t}{R_2C}}\mathrm{d}\tau \end{array}\right] \tag{B2}$$

$$P_{\mathrm{b}}(t)=I(t,P_{\mathrm{b}})\times \left[\begin{array}{l} V\left(\dfrac{1}{C_{\mathrm{N}}}\displaystyle\int_0^t I(\tau,P_{\mathrm{b}})\mathrm{d}\tau\right)\cdots+ \\ I(t,P_{\mathrm{b}})R_{\mathrm{l}}+\dfrac{1}{C_{\mathrm{N}}}\displaystyle\int_0^t I(\tau,P_{\mathrm{b}})\mathrm{e}^{\frac{\tau-t}{R_2C}}\mathrm{d}\tau \end{array}\right] \tag{B3}$$

From [(B2)–(B3)]/λ, then making $\lambda\to 0^+$, the left side of the equation yields:

$$\Delta P_{\mathrm{b}}(t)=\lim_{\lambda\to 0^+}\frac{P_{\mathrm{b}}(t)+\lambda\Delta P_{\mathrm{b}}(t)-P_{\mathrm{b}}(t)}{\lambda} \tag{B4}$$

Additionally, as $\lambda\to 0^+$, the following relationship between ΔP_{b} and ΔI is obtained:

$$\Delta I(t)=\frac{\partial I(t,P_{\mathrm{b}})}{\partial P_{\mathrm{b}}}\Delta P_{\mathrm{b}}(t)=\lim_{\lambda\to 0^+}\frac{I(t,P_{\mathrm{b}}+\lambda\Delta P_{\mathrm{b}})-I(t,P_{\mathrm{b}})}{\lambda} \tag{B5}$$

By iteratively substituting (B5) into (B4), equation (37) can be proved.

APPENDIX C

$$\begin{cases} H_\alpha(t) \triangleq V\left(\dfrac{1}{C_{\mathrm{N}}}\displaystyle\int_0^t I(\tau,P_{\mathrm{b}})\mathrm{d}\tau\right)+2I(t,P_{\mathrm{b}})R_\Omega+ \\ \qquad \dfrac{1}{C_{\mathrm{P}}}\displaystyle\int_0^t I(\tau,P_{\mathrm{b}})\mathrm{e}^{\frac{\tau-t}{R_{\mathrm{P}}C_{\mathrm{P}}}}\mathrm{d}\tau \\ H_\beta(t) \triangleq \dfrac{I(t,P_{\mathrm{b}})}{C_{\mathrm{N}}}V'\left(\dfrac{1}{C_{\mathrm{N}}}\displaystyle\int_0^t I(\tau,P_{\mathrm{b}})\mathrm{d}\tau\right) \\ H_\gamma(t) \triangleq \dfrac{I(t,P_{\mathrm{b}})}{C_{\mathrm{p}}} \end{cases} \tag{C1}$$

APPENDIX D

In (44), the coefficient polynomial of $\Delta I(t)$ is defined as:

$$H_\Sigma(t) \triangleq H_\alpha(t)+H_\beta(t)+H_\gamma(t) \tag{D1}$$

In (44), the trailing polynomial that includes the current correction information for times (1, t–1) is defined as:

$$\begin{cases} \theta(t)_{(t>1)} \triangleq \displaystyle\sum_{\tau=1}^{t-1}\Delta I(\tau)\left(H_\beta(t)+H_\gamma(t)\mathrm{e}^{\frac{\tau-t}{R_{\mathrm{P}}C_{\mathrm{P}}}}\right) \triangleq \\ \qquad \displaystyle\sum_{\tau=1}^{t-1}\Delta I(\tau)\varphi(\tau-t,t) \\ \theta(t)_{(t=1)}=0 \end{cases} \tag{D2}$$

APPENDIX E

$$\begin{cases} \mu(t) \triangleq -\dfrac{H_{\Sigma 1}(t)}{H_{\Sigma 2}(t)}\dfrac{\eta_2(t)}{\eta_1(t)} \\ \varepsilon(t) \triangleq -\dfrac{1}{H_{\Sigma 2}(t)}\dfrac{\eta_2(t)}{\eta_1(t)} \\ \nu(t) \triangleq -\dfrac{1}{H_{\Sigma 2}(t)} \\ \delta(t) \triangleq \dfrac{\eta_2(t)}{H_{\Sigma 2}(t)}\Delta P(t) \end{cases} \tag{E1}$$

ACKNOWLEDGMENT

Not applicable.

AUTHORS' CONTRIBUTIONS

Gan Guo: conceptualization, methodology, software, validation, writing original draft, and resources. Junhui Li: writing-review & editing, and supervision. Gang Mu: conceptualization, methodology, resources, and project administration. Gangui Yan: data curation and funding acquisition. All authors read and approved the final manuscript.

FUNDING

This work is supported by Key Program of the National Natural Science Foundation of China (No. 52337004).

AVAILABILITY OF DATA AND MATERIALS

Not applicable.

DECLARATIONS

Competing interests: The authors declare that they have no known competing financial interests or personal relationships that could have appeared to influence the work reported in this article.

AUTHORS' INFORMATION

Gan Guo received the Ph.D. degree in electrical engineering from Northeast Electric Power University. He is currently a postdoctoral researcher at Nanchang University. His research interests include vehicle-to-grid technology, energy storage systems, and renewable energy systems.

Junhui Li Received his Ph.D. degree at North China Electric Power University in 2012, received his M.S. degree at Northeast Electric Power University in 2003, received his B.S. degree at Northwestern Polytechnical University in 1998. He is teaching at Northeast Electric Power University and serving as the deputy director of the Ministry of Education Key Laboratory of Modern Power System Simulation Control and Green Power

New Technology. His research interests include planning and operation control of energy storage technology in power system.

Gang Mu received the Ph.D. degree in electrical engineering from Tsinghua University, China, in 1991. He is currently a professor at the Northeast Electric Power University, China. His research interests include power system stability analysis, planning, and the operation analysis of large-scale wind farms integration with power systems; planning and control of energy storage; and big data/AI applications in power system operations.

Gangui Yan is born in Jiangxi, China, in 1971. He received the Ph.D. degree from Tsinghua University in 2003. He is a professor and Ph.D. supervisor at Northeast Electric Power University. His current research interests include renewable energy system, energy storage system and power electronic technique, stability analysis and control of grid-connected renewable generations.

REFERENCES

[1] A. Kwade, W. Haselrieder, and R. Leithoff *et al.*, "Current status and challenges for automotive battery production technologies," *Nature Energy*, vol. 3, no. 4, pp. 290-300, Apr. 2018.

[2] S. Ge, Y. Leng, and T. Liu *et al.*, "A new approach to both high safety and high performance of lithium-ion batteries," *Science advances*, vol. 6, no. 9, Feb. 2020.

[3] H. Couzin, A. Ioannou, and K. Seyboth, "Renewables 2023 global status report," REN21 Sec., Paris, FR, Tech. Rep. RE-005(GSR-2023), 2023.

[4] U. S. E. I. Administration, (2021, Feb) "Utility-scale batteries and pumped storage return about 80% of the electricity they store," EIA, Washington DC, USA, [Online]. Available: https://www.eia.gov/todayinenergy/detail.php?id=46756

[5] X. Zhu, (2024, Apr.), "The first national-level photovoltaic and energy storage empirical experimental platform has achieved fruitful results," CEN, Beijing, China, [Online]. Available: https://doi.org/10.28693/n.cnki.nshca.2024.000373

[6] H. Shu, W. Li, and G. Wang *et al.*, "Online collaborative estimation technology for SOC and SOH of frequency regulation of a lead-carbon battery in a power system with a high proportion of renewable energy," *Protection and Control of Modern Power Systems*, vol. 9, no. 1, pp. 52-64, Jan. 2024.

[7] S. Pattnaik, M. R. Kumar, and S. K. Mishra *et al.*, "A review on characterization of supercapacitors and its efficiency analysis for different charging methods and applications," *Energy Storage*, vol. 5, no. 4, Aug. 2023.

[8] A. O. M. Maka and T. N. Chaudhary, "Performance investigation of solar photovoltaic systems integrated with battery energy storage," *Journal of Energy Storage*, vol. 84, Apr. 2024.

[9] A. Zurfi, A. A. R. Altahir, and G. Albayati *et al.*, "Energy loss evaluation of a battery buffered smart load controller," *Journal of Energy Storage*, vol. 42, Jul. 2021.

[10] S. Velamuri, S. H. C. Cherukuri, and S. K. Sudabattula, *et al.*, "Combined approach for power loss minimization in distribution networks in the presence of gridable electric vehicles and dispersed generation," *IEEE Systems Journal*, vol. 16, pp. 3284-3295, May 2022.

[11] E. Arnieri, L. Boccia, and F. A. Amoroso *et al.*, "Improved efficiency management strategy for battery-based energy storage systems," *Electronics*, vol. 8, no. 12, Dec. 2019.

[12] M. Schimpe, C. Piesch, and H. C. Hesse *et al.*, "Power flow distribution strategy for improved power electronics energy efficiency in battery storage systems: development and implementation in a utility-scale system," *Energies*, vol. 11, no. 3, Mar. 2018.

[13] A. J. Pimm, J. Palczewski, and R. Morris *et al.*, "Community energy storage: a case study in the UK using a linear programming method," *Energy Conversion and Management,* vol. 205, Feb. 2020.

[14] M. Schimpe, M. Naumann, and N. Truong *et al.*, "Energy efficiency evaluation of a stationary lithium-ion battery container storage system via electro-thermal modeling and detailed component analysis," *Applied Energy*, vol. 210, pp. 211-229, Jan. 2018.

[15] G. Smdani, M. R. Islam, and A. N. A. Yahaya *et al.*, "Performance evaluation of advanced energy storage systems: a review," *Energy & Environment*, vol. 34, no. 4, pp. 1-48, Jan. 2022.

[16] T. Katrašnik, I. Mele, and K. Zelič, "Multi-scale modelling of lithium-ion batteries: from transport phenomena to the outbreak of thermal runaway," *Energy Conversion and Management*, vol. 236, Apr. 2021.

[17] S. Wang, H. Gao, and P. Takyi-Aninakwa *et al.*, "Improved multiple feature-electrochemical thermal coupling modeling of lithium-ion batteries at low-temperature with real-time coefficient correction," *Protection and Control of Modern Power Systems*, vol. 9, no. 3, pp. 157-173, May 2024.

[18] C. Sheng, J. Fu, and D. Li *et al.*, "Energy management strategy based on health state for a PEMFC/lithium-ion batteries hybrid power system," *Energy Conversion and Management*, vol. 271, Nov. 2022.

[19] L. Chen, S. Wang, and H. Jiang *et al.*, "A multi-time-scale framework for state of energy and maximum available energy of lithium-ion battery under a wide operating temperature range," *Applied Energy*, vol. 355, Feb. 2024.

[20] M. A. Bamdezh and G. R. Molaeimanesh, "Aging behavior of an electric vehicle battery system considering real drive conditions," *Energy Conversion and Management*, vol. 304, Mar. 2024.

[21] J. Chen, Y. Zhang, and J. Wu *et al.*, "SOC estimation for lithium-ion battery using the LSTM-RNN with extended input and constrained output," *Energy*, vol. 262, Jan. 2023.

[22] A. J. Gonzalez-Castellanos, D. Pozo, and A. Bischi, "Non-ideal linear operation model for Li-ion batteries," *IEEE Transactions on Power Systems*, vol. 35, no. 1, pp. 672-682, Jan. 2020.

[23] J. Ahn and B. K. Lee, "High-efficiency adaptive-current

charging strategy for electric vehicles considering variation of internal resistance of lithium-ion battery," *IEEE Transactions on Power Electronics*, vol. 34, no. 4, pp. 3041-3052, Apr. 2019.

[24] S. Tamilselvi, S. Gunasundari, and N. Karuppiah *et al.*, "A review on battery modelling techniques," *Sustainability*, vol. 13, no. 18, Sep. 2021.

[25] O. Sadeghian, A. Oshnoei, and B. Mohammadi-ivatloo *et al.*, "A comprehensive review on electric vehicles smart charging: Solutions, strategies, technologies, and challenges," *Journal of Energy Storage*, vol. 54, Oct. 2022.

[26] X. Huang, W. Liu, and A. B. Acharya *et al.*, "Effect of pulsed current on charging performance of lithium-ion batteries," *IEEE Transactions on Industrial Electronics,* vol. 69, no. 10, pp. 10144-10153, Oct. 2021.

[27] B. Kwak, M. Kim, and J. Kim, "Add-on type pulse charger for quick charging Li-ion batteries," *Electronics*, vol. 9, no. 2, Jan. 2020.

[28] S. Zhu, C. Hu, and Y. Xu *et al.*, "Performance improvement of lithium-ion battery by pulse current," *Journal of Energy Chemistry,* vol. 46, pp. 208-214, Jul. 2020.

[29] W. Li, H. Wang, and X. He, "Distributed neurodynamic optimization for multi-energy management with time-varying external disturbances considering time-varying emission limitations and load demand in multi-microgrid," *ISA Transactions*, vol. 139, pp. 337-356, Aug. 2023.

[30] W. Zhu and Q. Wang, "Distributed finite-time optimization of multi-agent systems with time-varying cost functions under digraphs," *IEEE Transactions on Network Science and Engineering*, vol. 11, no. 1, pp. 556-565, Jan. 2024.

[31] J. M. Cano, N.-R. Ángel, and A. Suárez *et al.*, "Variable switching frequency control of distributed resources for improved system efficiency," *IEEE Transactions on Industry Applications*, vol. 54, no. 5, pp. 4612-4620, Sep. 2018.

[32] F. Corti, A. Laudani, and G. M. Lozito *et al.*, "Modelling of a pulse-skipping modulated DC–DC buck converter," *IET Power Electronics*, vol. 16, no. 2, pp. 243-254, Oct. 2023.

[33] C. Li, M. Zhou, and H. Wang, "An H5-bridge-based asymmetric LLC resonant converter with an ultrawide output voltage range," *IEEE Transactions on Industrial Electronics*, vol. 67, no. 11, pp. 9503-9514, Nov. 2020.

[34] J. Khodabakhsh and G. Moschopoulos, "A T-type DC-DC converter with reduced middle-leg switch current stress and improved light-load efficiency," *IEEE Open Journal of Power Electronics,* vol. 1, pp. 238-249, Jul. 2020.

[35] S. Zheng, G. Huang, and A. C. K. Lai, "Techno-economic performance analysis of synergistic energy sharing strategies for grid-connected prosumers with distributed battery storages," *Renewable Energy*, vol. 178, pp. 1261-1278, Nov. 2021.

[36] M. G. Choi, J. H. Choi, and S. Y. Yun *et al.*, "MILP-based service restoration method utilizing both existing infrastructure and ders in active distribution networks," *IEEE Access*, vol. 10, pp. 36477-36489, Apr. 2022.

[37] S. A. Amamra and J. Marco, "Vehicle-to-grid aggregator to support power grid and reduce electric vehicle charging cost," *IEEE Access*, vol. 7, pp. 178528-178538, Dec. 2019.

[38] N. Erdogan, F. Erden, and M. Kisacikoglu, "A fast and efficient coordinated vehicle-to-grid discharging control scheme for peak shaving in power distribution system," *Journal of Modern Power Systems and Clean Energy*, vol. 6, no. 3, pp. 555-566, Jan. 2018.

[39] S. Li, P. Zhao, and C. Gu *et al.*, "Battery protective electric vehicle charging management in renewable energy system," *IEEE Transactions on Industrial Informatics,* vol. 19, no. 2, pp. 1312-1321, Feb. 2023.

[40] C. Chiñas-Palacios, C. Vargas-Salgado, and J. Aguila-Leon *et al.*, "A cascade hybrid PSO feed-forward neural network model of a biomass gasification plant for covering the energy demand in an AC microgrid," *Energy Conversion and Management*, vol. 232, Mar, 2021.

[41] S. A. Vanfossan, "Advances and applications in high-dimensional heuristic optimization," Ph.D. dissertation, Engineering Management and Systems Engineering, Missouri University of Science and Technology, Rolla, USA, 2022.

[42] A. Simonetto, E. Dall'Anese, and S. Paternain *et al.*, "Time-varying convex optimization: time-structured algorithms and applications," *Proceedings of the IEEE,* vol. 108, no. 11, pp. 2032-2048, Nov. 2020.

[43] O. S. P. O.S and S. P. Lushchin, "Improvement of the evaluation method of calculation of power losses in power transformer," *Electrical Engineering and Power Engineering*, vol.4, no. 2, pp. 32-39, Dec. 2020.

[44] H. Kim, J. Maeng, and I. Park *et al.*, "A 90.2% peak efficiency multi-input single-inductor multi-output energy harvesting interface with double-conversion rejection technique and buck-based dual-conversion mode," *IEEE Journal of Solid-State Circuits*, vol. 56, no. 3, pp. 961-971, Mar. 2021.

[45] Erdiwansyah, Mahidin, and H. Husin *et al.*, "A critical review of the integration of renewable energy sources with various technologies," *Protection and Control of Modern Power Systems*, vol. 6, no. 1, pp. 1-18, Jan. 2021.

[46] J. Li, G. Mu, and J. Zhang *et al.*, "Dynamic economic evaluation of hundred megawatt-scale electrochemical energy storage for auxiliary peak shaving," *Protection and Control of Modern Power Systems*, vol. 8, no. 3, pp. 1-18, Jul. 2023.